JGR Solid Earth

RESEARCH ARTICLE
10.1029/2022JB025592

Numerical Modeling of Gas Hydrate Recycling in Complex Media: Implications for Gas Migration Through Strongly Anisotropic Layers

A. Peiraviminaei[1], S. Gupta[2], and B. Wohlmuth[1]

[1]Department of Mathematics, Technical University of Munich, Munich, Germany, [2]GEOMAR Helmholtz Center for Ocean Research Kiel, Kiel, Germany

Key Points:

- Structural heterogeneity linked to inclined fault systems or anomalous sediment layers have a strong impact on the gas hydrate dynamics
- The presence of anomalous high-permeability layers within gas hydrate stability zone alters the recycling process through flow-localization
- The presented discontinuous Galerkin scheme is able to accurately capture the gas hydrate recycling processes through strongly anisotropic materials

Correspondence to:
A. Peiraviminaei,
peiravim@ma.tum.de

Citation:
Peiraviminaei, A., Gupta, S., & Wohlmuth, B. (2022). Numerical modeling of gas hydrate recycling in complex media: Implications for gas migration through strongly anisotropic layers. *Journal of Geophysical Research: Solid Earth*, *127*, e2022JB025592. https://doi.org/10.1029/2022JB025592

Received 13 SEP 2022
Accepted 25 OCT 2022

Author Contributions:
Conceptualization: A. Peiraviminaei, S. Gupta, B. Wohlmuth
Data curation: A. Peiraviminaei
Formal analysis: S. Gupta, B. Wohlmuth
Investigation: S. Gupta, B. Wohlmuth
Methodology: A. Peiraviminaei, B. Wohlmuth
Project Administration: S. Gupta, B. Wohlmuth
Resources: S. Gupta, B. Wohlmuth
Software: A. Peiraviminaei, S. Gupta
Supervision: S. Gupta, B. Wohlmuth
Validation: S. Gupta, B. Wohlmuth
Visualization: A. Peiraviminaei, B. Wohlmuth
Writing – original draft: A. Peiraviminaei

Abstract Burial driven recycling is an important process in the natural gas hydrate (GH) systems worldwide, characterized by complex multiphysics interactions like gas migration through an evolving gas hydrate stability zone (GHSZ), competing gas-water-hydrate (i.e., fluid-fluid-solid) phase transitions, locally appearing and disappearing phases, and evolving sediment properties (e.g., permeability, reaction surface area, and capillary entry pressure). Such a recycling process is typically studied in homogeneous or layered sediments. However, there is mounting evidence that structural heterogeneity and anisotropy linked to normal and inclined fault systems or anomalous sediment layers have a strong impact on the GH dynamics. Here, we consider the impacts of such a structurally complex media on the recycling process. To capture the properties of the anomalous layers accurately, we introduce a fully mass conservative, high-order, discontinuous Galerkin (DG) finite element based numerical scheme. Moreover, to handle the rapidly switching thermodynamic phase states robustly, we cast the problem of phase transitions as a set of variational inequalities, and combine our DG discretization scheme with a semi-smooth Newton solver. Here, we present our new simulator, and demonstrate using synthetic geological scenarios, (a) how the presence of an anomalous high-permeability layer, like a fracture or brecciated sediment, can alter the recycling process through flow-localization, and more importantly, (b) how an incorrect or incomplete approximation of the properties of such a layer can lead to large errors in the overall prediction of the recycling process.

Plain Language Summary Gas hydrates are complex geosystems characterized by highly coupled multiphysics processes. Natural gas hydrates play an important role in the global carbon cycle and are also seen as a potential energy resource. A key question is *how* and *where* they form in nature, and *how much* hydrate there is in the world today. One of the common processes responsible for their formation is the burial driven recycling, where sedimentation continuously buries the GH layer and upward migrating free gas below the GHSZ, leading to distinct GH layers with high saturation in the vicinity of the base of the GHSZ. Simulation of the GH recycling process has many numerical challenges like solid-fluid and fluid-fluid phase transitions, rapidly switching phase states, appearing and disappearing phases, evolving sediment properties, and highly complex structure of the geological subsurface. In this manuscript, we particularly focus on the complex subsurface structure. We present a numerical scheme based on the DG finite element method which can handle full material anisotropies. Our results show that the presence of strongly anisotropic material anomalies (like faults) leads to a focused chimney like gas flow path, and an incorrect handling of such material anomalies can lead to completely different dynamical behavior.

1. Introduction

Methane hydrates are one of the most complex natural geosystems whose formation and dynamics is characterized by a wide range of strongly coupled and competing multi-physics processes such as gas migration through an evolving GHSZ, rapidly changing pressure-temperature-salinity fields, gas-water-hydrate (i.e., fluid-fluid-solid) phase transitions, locally appearing and disappearing phases, and evolving sediment properties (like permeability, capillary pressure, effective flow pathways, reaction surface area, etc.). Methane hydrates form an organic carbon repository in the earth, and have a significant contribution to the global carbon cycle. Besides, methane is an important greenhouse gas with drastic implications for climate (De La Fuente et al., 2022; Wuebbles et al., 2017), such as global warming, ocean acidification and de-oxygenation (Biastoch et al., 2011; Dickens, 2003). It has been estimated that the amount of carbon trapped in gas hydrates is more than twice the amount available in all other

Writing – review & editing: A. Peiraviminaei, S. Gupta

fossil fuels combined (Archer et al., 2009; Burwicz et al., 2011; Piñero et al., 2013), which has led to an increasing interest in gas hydrates as a potential energy resource (Boswell & Collett, 2011; Collett et al., 2009). Due to massive over-pressure generation, salt water freshening, and/or changes in sediment mechanical characteristics upon destabilization, gas hydrates have also been linked to local and regional slope failures (Geissler et al., 2015; Grozic, 2010) and other subsurface features like pockmarks and pingos (Ostanin et al., 2013; Riboulot, 2018; Serié et al., 2012; Waage et al., 2019), pipes and chimneys (Crutchley et al., 2021; Kang et al., 2015; Paganoni et al., 2018; Yoo et al., 2013), and salt domes and diapirism (Lewis & Sager, 2012), among others. It is, therefore, abundantly clear that gas hydrates play a crucial role in the solid Earth system.

A key question in nearly any study of the dynamics and impacts of gas hydrates is that of its *distribution*: How does it form, where does it form, how did it evolve over gelogical time scales, and how much does it exist today? Sedimentary organic matter in the deep biosphere generates biogenic and thermogenic methane gas due to microbial biodegradation and elevated temperature and pressure. This generated methane migrates upward toward the sea-floor as a free gas or by advection of the porewater. Methane hydrates form where sufficient methane reaches the GHSZ where pressure, temperature, and salinity allow the formation of hydrate (Schmidt et al., 2022; You et al., 2019) for example, in the permafrost regions and the marine sediments in the oceans and deep lakes. However the continuous sedimentation over geological time scales pushes this layer below the stability zone where methane gas is released and flows back to the new GHSZ. This process of burial-driven recycling of gas hydrates is believed to generate a high methane hydrate saturation which is economically interesting for gas production for example, in the Gulf of Mexico with saturation of up to 90% (Flemings et al., 2020). Although the upward flow of methane gas into the GHSZ is, in general, blocked, as hydrates fill pore volumes and fractures (Burwicz et al., 2017; Nimblett & Ruppel, 2003), methane can still escape from hydrate layers within the GHSZ and reach the sea-floor (Liu & Flemings, 2006) which has huge environmental impacts. Infact, Schmidt et al. have shown that the GH layers act as a mechanical nozzle in the path of upward migrating gas where, given sufficient free gas below the hydrate layer, the gas hydrate peak acts as the throat of the nozzle and divides the gas hydrate layer into a converging part (below the throat) where gas experiences deceleration, and a diverging part (above the throat) where gas experiences acceleration (Schmidt et al., 2022). This GH-nozzle introduces an interesting dynamics that leads to a *cyclic* rebuilding of the gas hydrate layers under continuous burial.

Given the vast complexity of the gas hydrate systems, the modeling of gas hydrate dynamics in general, and burial-driven recycling in particular, poses multiple conceptual and computational challenges. One interesting challenge that is central to gas hydrate dynamics is that of gas-water-hydrate phase transitions. In such situations methane can dissolve into and exsolve from porewater leading to a locally appearing and disappearing free-gas phase, and the gas hydrates can melt or precipitate, leading to an appearing, disappearing, and evolving solid phase. These fluid-fluid and fluid-solid interactions occur at different time scales, for example, methane dissolution-exsolution is a fast process governed by vapor-liquid equilibrium on the geological time scales, while gas hydrate phase change is a slower process where the equilibrium assumption may not hold under rapid sedimentation, and is therefore, modeled as a kinetically controlled process (Gupta et al., 2020). These phase transitions are in permanent competition that drives the aforementioned *cyclic* rebuilding of gas hydrates.

The numerical challenges related to the phase transitions are discussed in (Class et al., 2006; Marchand et al., 2013). Different numerical techniques have been constructed to overcome the phase transitions in multi-phase multi-components porous media models, for example, primary variable switching (PVS) (Class et al., 2002; Wu & Forsyth, 2001), negative saturations (Panfilov & Panfilova, 2014), method of persistent variables (Huang et al., 2015; Neumann et al., 2013) and non-linear complementary problem approaches (Ben Gharbia & Jaffré, 2014; Kräutle, 2011; Lauser et al., 2011). PVS schemes are implemented in many of the hydrate reservoir simulators such as TOUGH-Hydrate (Moridis et al., 2008). Gupta et al. (Gupta et al., 2020) extended the non-linear complementary constraints approach of (Lauser et al., 2011) to gas hydrate systems, and showed that under rapidly switching phase states, this approach seems to be capable of handling the gas-water-hydrate phase transitions more accurately, robustly, and efficiently compared to the more traditional PVS schemes. Furthermore, with the help of this newly developed simulator, Schmidt et al. (2022) were able to demonstrate the mechanics of the *hydrate nozzle* and its implications for gas migration through GHSZ during continuous burial.

Conventionally, gas hydrate recycling has been largely studied in 1D geological settings and the underlying sediments are assumed to be either homogeneous (Schmidt et al., 2022) or with vertically stacked topography (You et al., 2019, 2021) that is representative of the different granular materials, debris, and organic matter that was

deposited over different geological times in the past. However, complex fault systems, fluid escape structures, and anomalous sediment layers have been observed in the seismic profiles cross-cutting the buried layers within the GHSZ worldwide (Crutchley et al., 2021; Paganoni et al., 2018; Portnov et al., 2019; Waage et al., 2019). In fact, the formation and propagation of focused flow pathways (pipes, chimneys) and their implications on gas migration, hydrate dynamics, and slope stability remains an important open question. Numerically, handling such anomalous layers is quite challenging and computationally expensive in terms of how the heterogeneity and anisotropy is physically modeled, how the numerical scheme approximates the related fluxes and any material interfaces and/or discontinuities. In the past, we have used the cell centered finite volume (FV) methods for numerical discretization of our gas hydrate models (Gupta et al., 2015, 2020) because of their inherent simplicity for implementation of non-linear complementary problems (NCP), local mass conservation property, monotonicity, and low computational costs due to their low order and small two-point stencils. While FV methods offer a very robust, efficient, and reliable numerical framework for simple geological media, it is notoriously difficult to extend to unstructured meshes, fully anisotropic media, and discontinuous material interfaces. Forms of finite element (FE) (Cheng et al., 2013; Fang, 2010) and finite difference (FD) (Holder & Angert, 1982; Yu et al., 2017) methods are also commonly used for methane hydrate models, but they also face challenges related to phase transitions, local mass conservation, overshoots and undershoots (which further complicate the phase change problem), mesh sizes and local mesh anisotropy, and material interfaces. The discontinuous Galerkin (DG) finite element method generalizes the FE method by omitting continuity constraints, allowing potential jumps through numerical fluxes (Cockburn et al., 2000). Moreover, DG methods are locally conservative and a consistent flux across the element interfaces can be easily constructed. Therefore, DG methods, which are generalization of both FV and FE methods, appear to be more suitable for the numerical solution of the methane hydrate model not only because it can handle complex geometries and meshes (including hanging nodes), full material anisotropies, and jumps across material interfaces in a natural manner without additional computational overheads, but also because it preserves the local mass conservation property of the FV method while at the same time provides higher order approximations like FE methods. Moreover, DG schemes offer massive parallelization capability (Bey et al., 1996), which is very important for practical applications. In this manuscript, we, therefore, present a DG-based numerical scheme for our gas hydrate model, extended with the NCP-based semi-smooth Newton solver to handle the inequality constraints related with the phase transitions. In Section 2, we present the methane hydrate model based on Gupta et al. (2020). In Section 3, we outline our numerical algorithm based on the DG discretization scheme summarized in Appendix A. Finally, in Section 4, we present our numerical results. First, we validate the numerical scheme and its implementation by considering a 1D scenario of burial-driven recycling that was analyzed in Gupta et al. (2020), and second we simulate synthetic 2D scenarios of burial-driven recycling with different configurations of anomalous anisotropic high-permeability layers in the path of upward migrating gas. With these numerical examples, we demonstrate the numerical capabilities of our DG-scheme, and also highlight the necessity of modeling such layers with precision and care.

2. Mathematical Model

We consider the gas hydrate model developed by Gupta et al. (2020). The representative elementary volume (REV) for the model is shown in Figure 1, (Gupta et al., 2020).

This model is based on the theory of porous media and accounts for the following multiphysics processes:

a) Dynamic evolution of the GHSZ due to changes in thermodynamic pressure-Temperature-Salinity (pTS) states,
b) Migration of dissolved and gaseous methane through evolving GHSZ,
c) Rate-based gas hydrate phase transitions,
d) Exsolution-dissolution of methane in pore-water, and associated appearance and disappearance of free gas phase,
e) Thermal effects, including the heat of hydrate phase change,
f) Salinity changes, including feedbacks on methane solubility as well as hydrate stability,
g) Changing sediment properties due to changes in pore-voids due to hydrate phase changes.

Moreover, we assume that salt is not allowed to precipitate as solid phase, sediment porosity is constant, that is, sediment compaction is neglected. A detailed model description including underlying assumptions can be found in Gupta et al. (2020). In the following, a summary of the main governing and constitutive equations is presented.

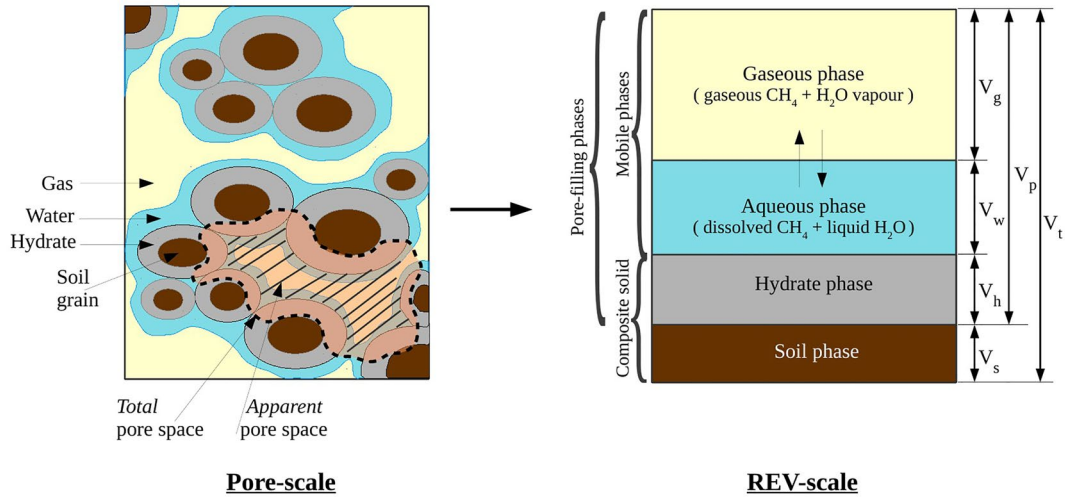

Figure 1. Representation of the phases and components in a representative elementary volume (REV) from Gupta et al. (2020). Porosity: $\phi = \frac{V_p}{V_t}$; Phase Saturation: $s_\beta = \frac{V_\beta}{V_p}$, $\beta = g, w, h$; Mole Fraction: $\chi_\alpha^\kappa = \frac{n_\alpha^\kappa}{\sum_\kappa n_\alpha^\kappa}$, $\kappa = CH_4, H_2O, c$, $\alpha = g, w$, where n_α^κ is the number of moles of the component κ in phase α.

Let Ω be a bounded domain which contains the porous medium where the methane hydrate recycling (MHR) occurs. We assume that Ω is a subset of $\mathbb{R}^d$, $d \in \{1, 2\}$ and has smooth boundary (Lipschitz boundary). $\partial\Omega_D$ and $\partial\Omega_N$ denote the Dirichlet and Neumann parts of the boundary respectively and $\mathbb{T} := [0, t_{end}]$ denotes the time interval. Subscript $\beta \in \{h, g, w\}$ denotes three pore-filling phases (gas(g), water(w) and hydrate (h)), subscript $\alpha \in \{g, w\}$ denotes two fluid phases (gas(g), water(w)), subscript s denotes the solid phase (sediment matrix), and superscript $\kappa \in \{M, H, c\}$ denotes three components (Methane(M), Water(H) and salts(c)) in a porous medium. We introduce the following functions as model variables,

$$\begin{aligned} s_\beta &: \Omega \times \mathbb{T} \to [0,1] && \text{Saturation of phase } \beta \\ \chi_\alpha^\kappa &: \Omega \times \mathbb{T} \to [0,1] && \text{Mole fraction of component } \kappa \text{ in phase } \alpha \\ p_\alpha &: \Omega \times \mathbb{T} \to \mathbb{R} && \text{Pressure distribution of phase } \alpha \\ T &: \Omega \times \mathbb{T} \to \mathbb{R} && \text{Temperature} \end{aligned} \tag{1}$$

Let $\mathbf{U}$ be the vector of model primary variables, which is some subset of the above introduced functions. We consider from the set of all model variables (Equation 1),

$$\mathbf{U} := \left(p_w, T, s_g, s_h, \chi_w^M, \chi_g^H, \chi_w^c\right) = (\mathbf{U}_1, \mathbf{U}_2, \ldots, \mathbf{U}_7) \tag{2}$$

as the primary variables.

2.1. Mass and Momentum Balance

Mass and momentum balance equations in a porous media for the components κ can be written as follows:

$$\begin{aligned} A^\kappa(\mathbf{U}) := &\sum_\alpha \partial_t(\phi\, \rho_\alpha\, \chi_\alpha^\kappa\, s_\alpha) + \sum_\alpha \nabla.(\rho_\alpha\, \chi_\alpha^\kappa\, \mathbf{v}_\alpha) \\ &+ \sum_\alpha \nabla.(\phi\, s_\alpha\, \mathbf{J}_\alpha^\kappa) - \dot{g}^\kappa = 0, \quad \text{in } \Omega \times \mathbb{T} \end{aligned} \tag{3}$$

where ρ_α and μ_α are the density and dynamic viscosity of the fluid phase α with velocity $\mathbf{v}_\alpha$ relative to primary sediment matrix. $\mathbf{J}_\alpha^\kappa$ is diffusion flux of the component κ through fluid phase α. The time derivative terms accounts for the rate of change of the total mass of the component κ in each fluid phase α (χ_α^κ). The second and the third

terms of Equation 3 give the amount of advection and diffusion of χ_α^κ and $\dot{g}^\kappa$ is the volumetric source resulting from the hydrate phase change. Furthermore, we assume that there is no salt in the gas phase, i.e., $\chi_g^c = 0$.

We assume that hydrate phase is immobile, that is, $\mathbf{v}_h = 0$. Mass balance equation for the hydrate phase is given by

$$A^h(\mathbf{U}) := \partial_t (\phi\, \rho_h\, s_h) - \dot{g}_h = 0, \quad \text{in } \Omega \times \mathbb{T} \tag{4}$$

Darcy's Law for the momentum balance of the fluid phase will be considered

$$\mathbf{v}_\alpha = -\mathbf{K}\, \frac{k_{r\alpha}}{\mu_\alpha}\, (\nabla p_\alpha - \rho_\alpha \mathbf{g})\,. \tag{5}$$

Ficks Law for the diffusive mass flux through the composite sediment matrix will be considered

$$\mathbf{J}_\alpha^\kappa = -\tau\, \mathbf{D}_\alpha^\kappa\, \rho_\alpha\, \nabla \chi_\alpha^\kappa, \tag{6}$$

where $k_{r\alpha}$ and $\mathbf{D}_\alpha^\kappa$ are relative permeability and molecular diffusion coefficient of the component κ through fluid phase α respectively. τ is the sediment tortuosity. Since $\chi_g^c = 0$ then $\mathbf{J}_g^c = 0$. In addition, we have

$$\sum_\kappa \mathbf{J}_\alpha^\kappa = 0. \tag{7}$$

2.2. Energy Balance

Energy balance equation is given by

$$\begin{aligned} A^e(\mathbf{U}) := \partial_t \left((1-\phi)\, \rho_s\, u_s + \phi \sum_\beta \rho_\beta\, u_\beta\, s_\beta \right) - \nabla . \left(k_{eff}^{th} \nabla T \right) \\ + \sum_\alpha \nabla . (\rho_\alpha\, h_\alpha\, \mathbf{v}_\alpha) - \dot{Q}_h = 0, \text{ in } \Omega \times \mathbb{T} \end{aligned} \tag{8}$$

where $\dot{Q}_h$ denotes heat of hydrate phase change and h_α is the specific enthalpy of fluid phase α, u_γ is the specific internal energy of the phase $\gamma = g, w, h,$ s, and k_{eff}^{th} is the effective thermal conductivity,

$$k_{eff}^{th} = (1-\phi)\, k_s^{th} + \sum_\beta \phi\, s_\beta\, k_\beta^{th}, \quad \beta = g, w, h. \tag{9}$$

2.3. Hydrate Phase Change Kinetics

We represent the rate of methane hydrate reaction, for a more detailed description see (Gupta et al., 2020). When methane hydrate is exposed to different effects such as depressurization or warming up, it decomposes to it's components. The rate of this reaction is modeled by the Kim-Bishnoi kinetic model (Kim et al., 1987). In this model, the rate of water and gaseous methane generated as a result of hydrate phase change are evaluated by

$$\dot{g}^M = k^r A_{rs} \mathbb{M}^M (p_e - p_g)\,, \quad \dot{g}^H = \dot{g}^M N_h \left(\frac{\mathbb{M}^H}{\mathbb{M}^M} \right), \tag{10}$$

where p_e is the equilibrium pressure for the methane hydrate, k^r is the intrinsic reaction rate of hydrate phase change, and A_{rs} is the reaction surface area available for hydrate phase change. $\mathbb{M}^\kappa$ is the molar mass of the component κ and N_h denotes the hydration number. If $(p_e - p_g) > 0$, the hydrate becomes unstable and If $(p_e - p_g) < 0$, the hydrate becomes stable. Hydrate stability means that $\dot{g}^M < 0$ and according to mass balance Equation 3, if gaseous methane exists, it will be trapped between the water molecules and methane hydrate forms (Hydrate formation). Conversely instability means that $\dot{g}^M > 0$ and if methane hydrate exits, it releases gaseous methane and water molecules (Hydrate dissociation). $\dot{g}_h$ denotes the hydrate formation (dissociation) rate. In addition, the following condition holds

$$\dot{g}^M + \dot{g}^H + \dot{g}_h = 0. \tag{11}$$

where $\dot{g}_h$ and the heat of hydrate phase change is given by

$$\dot{g}_h = -\dot{g}^M \left(\frac{\mathtt{M}_h}{\mathtt{M}^M}\right), \quad \mathtt{M}_h = \mathtt{M}^M + N_h \mathtt{M}^H, \quad \dot{Q}_h = \frac{\dot{g}_h}{\mathtt{M}_h}(a_1 + a_2 T). \tag{12}$$

2.4. Closure Relationships

The capillary pressure occurs across the gaseous and aqueous phase interface due to balancing of cohesive forces within the liquid and the adhesive forces between the liquid and soil matrix and relates the water and gas pressure.

$$p_g - p_w = p_c \tag{13}$$

Moreover, we have the following relation between phase saturations.

$$\sum_\beta s_\beta = 1, \tag{14}$$

that is, total pore space is filled with hydrate, aqueous, and gaseous phases.

2.5. Vapor-Liquid Equilibrium (VLE)

Methane and water components are assumed to exist in vapor-liquid equilibrium and Henry's law and Raoult's law are valid. These equations relate mole fractions of each component existing in different phases.

$$\text{Henry's law:} \quad z^M \chi_g^M p_g = H_w^M \chi_w^M \tag{15}$$

$$\text{Raoult's law:} \quad \chi_g^H p_g = P_{sat}^H \chi_w^H \tag{16}$$

where z^M is the compressibility factor for methane gas, evaluated using Peng-Robinson equation of state, H_w^M is the Henry's solubility coefficient for methane gas in water, and P_{sat}^H is the saturated vapor pressure for water in contact with methane gas. In addition to Equations 15 and 16, total mole fraction of components within each phase is bounded by 0 and 1, and it is 1 if the phase α is present, that is,

$$\sum_\kappa \chi_\alpha^\kappa = 1 \text{ if } s_\alpha > 0 \quad \text{and} \quad \sum_\kappa \chi_\alpha^\kappa < 1 \quad \text{if} \quad s_\alpha = 0 \tag{17}$$

The second inequality in Equation 17 holds when the corresponding phase disappears, that is, $s_\alpha = 0$, and because the VLE assumed to be valid, the mole fractions of the components remain undersaturated and are calculated from VLE Equations 15 and 16. We can write an equivalent complementarity conditions to the conditions in Equation 17

$$0 \le \sum_\kappa \chi_\alpha^\kappa \le 1, \quad 0 \le s_\alpha \le 1, \quad s_\alpha \left(1 - \sum_\kappa \chi_\alpha^\kappa\right) = 0. \tag{18}$$

Now we consider the nonlinear complementary problem for the inequality constraints (Equation 18):

$$A^{\text{ncp1}}(\mathbf{U}) := s_g - \max\left\{0,\ s_g - 1 + \sum_\kappa \chi_g^\kappa\right\} = 0 \text{ in } \Omega \times \mathbb{T}, \tag{19}$$

$$A^{\text{ncp2}}(\mathbf{U}) := s_w - \max\left\{0,\ s_w - 1 + \sum_\kappa \chi_w^\kappa\right\} = 0 \text{ in } \Omega \times \mathbb{T}. \tag{20}$$

2.6. Hydraulic Properties

Capillary pressure is parameterized using Brooks-Corey model (Brooks & Corey, 1964) and is given by

$$p_c = P_0\, s_{we}^{\frac{-1}{\lambda}} (1 - s_h)^{-\frac{m\lambda-1}{m\lambda}}, \tag{21}$$

where $s_{we} = \frac{s_w - S_{wr} - S_{gr}}{1 - s_h - S_{wr} - S_{gr}}$ denotes the normalized aqueous phase saturation and S_{wr} and Sgr are the irreducible aqueous and gaseous phase saturations respectively. Moreover, P_0 is the capillary entry pressure, λ is the material parameter related to sediment grain-size distribution, and m is the material parameter related to sphericity of hydrate growth.

Following the Brooks–Corey model, we parameterize the relative fluid phase permeabilities,

$$k_{rw} = s_{we}^{\frac{2+3\lambda}{\lambda}}, \quad k_{rg} = (1 - s_{we})^2 \left(1 - s_{we}^{\frac{2+\lambda}{\lambda}}\right). \tag{22}$$

Furthermore, we consider the effect of changing effective pore space due to hydrate phase change for the sediment permeability,

$$\mathbf{K} = \mathbf{K}_0 (1 - s_h)^{\frac{5m+4}{2m}}. \tag{23}$$

where $\mathbf{K}_0$ is the absolute permeability tensor of the primary sediment matrix. The exact functional relationships can be found in detail in (Gupta et al., 2020).

Let $C = \{M, H, h, c, e, ncp1, ncp2\}$ be the set of indices of the corresponding Equations 3, 4, 8, 19, and 20. We remark that the number of equations is equal to the number of primary variables and thus after discretization we obtain a quadratic matrix. Moreover, let $\partial\Omega_i^D \subseteq \partial\Omega$ and $\partial\Omega_i^N \subseteq \partial\Omega$ be the corresponding Dirichlet and Neumann boundary conditions for $\mathbf{U}_i$.

Then, we have the following nonlinear problem,

Problem 1. *Find* $\mathbf{U} : \Omega \times \mathbb{T} \to \mathbb{R}^7$ *such that*

$$\begin{aligned} \mathcal{A}(\mathbf{U}) &:= [A^i(\mathbf{U})]_{i \in C} = 0 \quad \text{in } \Omega \times \mathbb{T}, \\ \mathbf{U}(x, 0) &= \mathbf{U}^0 \qquad \text{in } \Omega, \\ \mathbf{U}_i(x, t) &= \mathbf{U}_i^D \qquad \text{on } \partial\Omega_i^D \times \mathbb{T}, \\ \nabla \mathbf{U}_i . \vec{n}_i &= \mathbf{U}_i^N \qquad \text{on } \partial\Omega_i^N \times \mathbb{T}, \end{aligned} \tag{24}$$

where $\mathbf{U}^0$, $\mathbf{U}_i^D$ *and* $\mathbf{U}_i^N$ *are given functions.*

Note that this problem is composed of a strongly coupled and highly nonlinear system of differential algebraic system of equations with four partial differential Equations 3, 8, one ordinary differential Equation 4, and two algebraic constraints (Equations 19–20).

3. Numerical Algorithm

Problem 1 is discretized in space using a DG method of order q defined on a quadrilateral mesh with $\mathbb{N}_h$ elements and mesh size h. A fully Implicit Euler (IE) method is used to discretize the ODE system resulting from the spatial DG discretization. A brief description of the discretization scheme is given in Appendix A. The resulting nonlinear residual equations can be represented in compact form as follows, (Equation A22):

$$\mathcal{R}\left(\mathbb{U}^{n+1}, \mathbb{U}^n\right) = 0, \qquad \mathbb{U}^{n+1},\ \mathbb{U}^n \in \mathbb{R}^{\mathbf{N}_h}, \tag{25}$$

where $\mathbb{U}^n$ is the solution vector at time t_n.

The nonlinear system (Equation 25) is linearized using a semi-smooth Newton solver, see (Wohlmuth, 2011) and references therein, which ensures that the rapidly switching phase states due to phase transitions remain consistent within each Newton step. In our scheme, we solve Equation 25 monolithically, that is, phase states will be determined along with solving the mass and energy balance equations. Within Newton loops, each phase state is determined by NCP Equations 19 and 20 which partitions the degrees of freedom (Dof) into active/inactive sets.

Algorithm 1. Newton Method, Adaptive Time Control.

Input: $\Delta t_{max} > \Delta t_0 > \Delta t_{min} > 0$, $tol > 0$, $j_{\max}, j_1, j_2 \in \mathbb{N}$, $\mathbb{U}^0$
Output: $\mathbb{U}^n$, $n = 1, 2, 3, \cdots$
$n \leftarrow 0$,
While $t_{n+1} \in \mathbb{T}$ **do** {
if $\Delta t_n < \Delta t_{\min}$ **do** {
stop ▷ *change the discretization parameters, see Appendix* (A)
}
$j \leftarrow 0$, $\mathbb{U}^{j,n+1} \leftarrow \mathbb{U}^n$ ▷ *initializing Newton method*
While $\|\mathcal{R}\left(\mathbb{U}^{j,n+1}\right)\| > tol$ **do** {
Solve $\mathcal{J}\left(\mathbb{U}^{j,n+1}\right)\mathbb{E}^k = -\mathcal{R}\left(\mathbb{U}^{j,n+1}\right)$ ▷ *linearization*
$\mathbb{U}^{j+1,n+1} \leftarrow \mathbb{U}^{j,n+1} + \mathbb{E}^j$
$j \leftarrow j + 1$
if $j > j_{\max}$ **do** {
$\Delta t_n \leftarrow (0.5 \times \Delta t_n)$ ▷ *reducing time step size*
restart from (3)
}
}
if $j < j_1$ **do** {
$\Delta t_{n+1} \leftarrow (1.2 \times \Delta t_n)$ ▷ *increasing time step size*
}
if $j_2 < j \leq j_{\max}$ **do** {
$\Delta t_{n+1} \leftarrow (0.8 \times \Delta t_n)$ ▷ *reducing time step size*
}
$\mathbb{U}^{n+1} \leftarrow \mathbb{U}^{j,n+1}$
$n \leftarrow n + 1$
}

These active/inactive sets may change during the Newton loop, but the convergence of the Newton method guarantees the physically correct phase state of the system. The classical Newton method is applicable in the subsets of $\mathbb{R}^{\mathbf{N}_h}$ where the functional $\mathcal{R}$ is differentiable. Algebraic Equations 19 and 20 are semi-smooth and piecewise differentiable. We extend the values of the derivatives from nondifferentiable to differentiable regions using central difference method to calculate the Jacobian for our Newton scheme. The Jacobian can be numerically calculated using directional derivative: the ith column of the Jacobian can be obtained by

$$\left[\mathcal{J}\left(\mathbb{U}^{n+1}\right)\right]_i \approxeq \frac{1}{2\epsilon}\left(\mathcal{R}\left(\mathbb{U}^{n+1} + \epsilon E_i, \mathbb{U}^n\right) - \mathcal{R}\left(\mathbb{U}^{n+1} - \epsilon E_i, \mathbb{U}^n\right)\right), \tag{26}$$

where $\epsilon > 0$ is a small positive number and $E_i \in \mathbb{R}^{\mathbf{N}_h}$, $i = 1, .., \mathbf{N}_h$ is the standard basis vector.

Time step sizes Δt_n are adaptively adjusted according to heuristical rules based on the Newton performance, that is, Δt_n increases by 20% if the Newton method converges in less than 5 iterations, decreases by 20% if the Newton method converges in more than 8 iterations, remains unchanged if the number of iterations of the Newton method is between 5 and 8, compared to Δt_{n-1}. If the Newton Solver does not converge within 10 iterations, then we redo the time step with a step length of $\frac{\Delta t_n}{2}$.

In the following, we outline our numerical algorithm 1 for solving Equation 25. $\mathbb{U}^0$ is the initial solution vector, j is the Newton iteration superscript, and $\mathcal{J}\left(\mathbb{U}^{jn}\right)$ is the Jacobian matrix of the residual vector $\mathcal{R}$ at $\mathbb{U}^{jn}$. Moreover, the algorithm contains the following numerical parameters: Δt_{max}, Δt_{min} → maximum and minimum time-steps allowed for the adaptive time-stepping; tol → maximum error accepted for the residual functional $\mathcal{R}$; j_{max} → maximum number of Newton steps considered at each time-step; j_1, j_2 → number of newton steps to adapt time-step sizes.

The numerical algorithm 1 is implemented using the software framework DUNE-PDElab (Bastian et al., 2010), version 2.7.0 (https://www.dune-project.org/modules/dune-pdelab/). To solve the linear system in line (1) of the algorithm, we use an in-built biconjugate gradient stabilized method (BiCGSTAB) (Blatt et al., 2016), as iterative solver for the linearized system. In all numerical examples presented in this manuscript, the parameters of the DG scheme in Appendix A and the numerical algorithm are chosen as

$$\begin{aligned} j_{\max} = 10, \quad j_1 = 4, \quad j_2 = 8, \quad tol = 10^{-6}, \\ \sigma_p = \sigma_s = \sigma_x = \sigma_T = 10, \qquad \Theta = 0. \end{aligned} \tag{27}$$

where σ is the penalty coefficient and Θ chooses the type of DG scheme ($\Theta = 1$ for symmetric DG scheme, $\Theta = 0$ for incomplete DG scheme, $\Theta = -1$ for non-symmetric DG scheme).

4. Numerical Results

Our main motivation for the development of this new simulation framework based on the DG method arose from the need for accurate and robust handling of the multiphysics dynamics of the MHR problems in complex geological media, especially in relation with large local anisotropy and material heterogeneities. Our existing simulation environment (Gupta et al., 2020) is based on a finite volume based numerical scheme which offers many advantages like being fully locally mass-conservative, monotonic (i.e., no overshoots and undershoots, even with coarse mesh), conceptually simpler (in terms of implementation of active/in-active sets related with the semi-smooth Newton method), and computationally cheaper (due to low order and therefore fewer degrees of freedom). However, it has a major limitation when the subsurface properties show large local anisotropies and other complex material properties such as cross-cutting features like fractures and brecciated layers. With that in mind, we present here two numerical examples: (a) Example 1 considers a simplified 1D MHR scenario in a fully homogeneous medium with continuous burial at a constant rate. This example is used as a *benchmark* to validate the implementation of our DG scheme against our FV simulator, and (b) Example 2 simulates MHR scenarios in a more complex 2D setting where two different configurations of idealized anomalous anisotropic material layers are considered in the GHSZ. The goal of Example 2 is to demonstrate the capability of our simulator in handling such complex sediment structures, and to highlight the impacts on prediction accuracy that can arise from incomplete and/or inaccurate approximation of the properties of these complex sediment structures. Material properties are given in Tables 3 and 4. For our simulations, the domain of interest remains constant, despite the sedimentation, that is, at time $t > 0$ top of our domain of interest is not sea floor and it shifts downwards, red box in Figure 2, for example, at time $t = 90$ Kyr, sedimentation depth is 90 m ($90{,}000 \times 0.001$), therefore, top boundary of the domain of interest lies at the depth of 90 m. In Figures 3, 4, and 6, we don't add sedimentation depth, because the goal is to see the evolution of the MHR process. Moreover, we consider hydrostatic pressure and local thermal equilibrium in both Examples inside the domain of interest.

Example 1. *Validation scenario: MHR in a homogeneous domain*

This scenario, developed and analyzed by Gupta et al. (2020), is based on the geological setting of a buried channel-levee (BCL) complex in the Danube paleo delta (Black Sea) that is believed to have deposited its levees between 320 and 75 kilo-annum before present (ka BP) (Zander et al., 2017). Here, we simulate how a continuous deposition of sediment layers over the past 300 ka could have affected the MHR though the gas hydrate stability zone (GHSZ). Hence, the initial setting is based on the paleo conditions existing at 300 ka BP, and the top of the computational domain is pinned at the corresponding paleo sea floor. We consider a 1D domain $\Omega = [-500, 0]$. The problem schematic is shown in Figure 2.

Initial and boundary conditions are specified in Table 1. At $t = 0$, we assume hydrostatic pressure at sea floor $p_w = 15\ MPa$ and a bottom water temperature of $T = 4°\ C$. We assumed that the initial pressure distribution within the computational domain follows a hydrostatic gradient, and the initial temperature distribution follows a steady-state geothermal gradient of 35° C/km. Moreover, water salinity is 3.5%. For detailed description of the initial and boundary conditions see (Gupta et al., 2020). For the prescribed paleo pTS conditions, the base of the GHSZ (bGHSZ) (i.e., depth at which $p_e = p_g$) lies at 400 m below sea floor (mbsf). At $t = 300$ ka BP, we assume that there is no free gas anywhere in the domain, and methane hydrate is located in the interval [320, 400] mbsf, directly above the bGHSZ. Furthermore, we assume that the deposition of the sediment layer at $z = 0$ (i.e., paleo

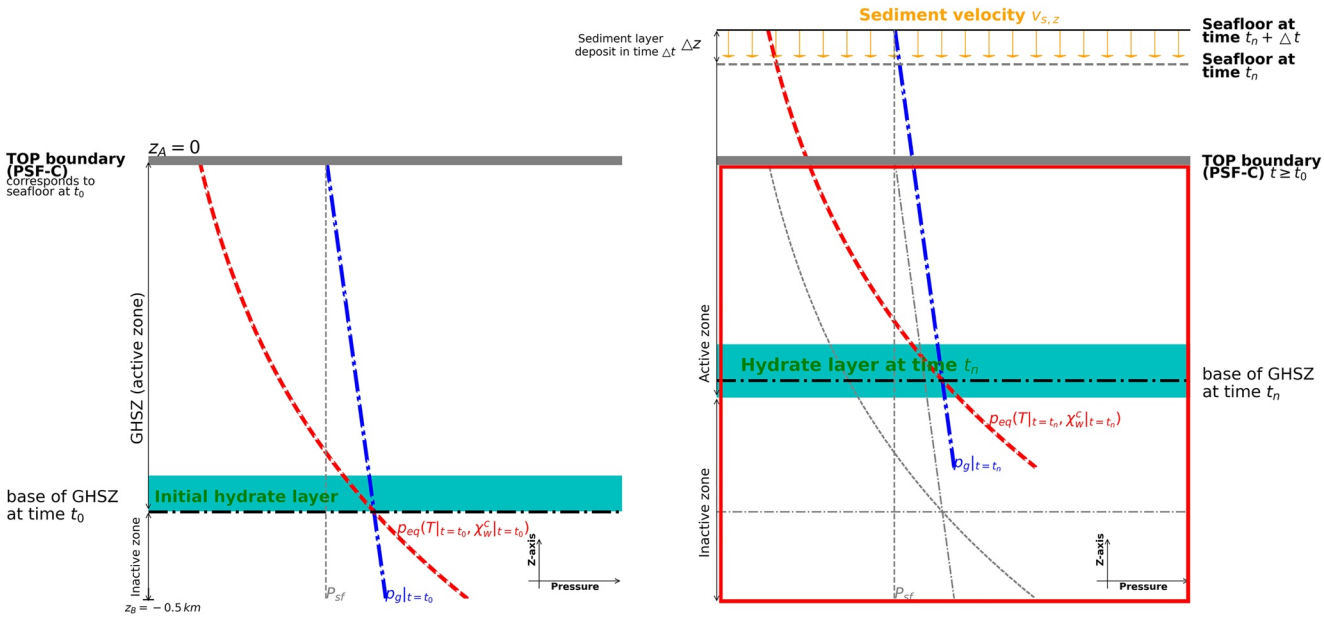

Figure 2. Problem setting for Example 1, recreated from Gupta et al. (2020). *left*: The initial state of the system and the corresponding hydrate layer inside the gas hydrate stability zone (GHSZ), $t = t_0 = 0$ (i.e., 300 ka BP). *right*: The state of the system at $t = t_n > 0$, indicating how the GHSZ shifts as a result of sedimentation over time. Note that the red box is the simulation domain for our 2D case.

sea floor) occurs with constant sedimentation rate $v_{s,z} = 1$ mm/year over a period of 300 ka (i.e., from 300 ka BP to present day).

As sedimentation occurs, more and more sediment layers accumulate above the paleo sea floor, leading to an increasing pressure and temperature at the paleo sea floor boundary. These changes cause the bGHSZ to shift

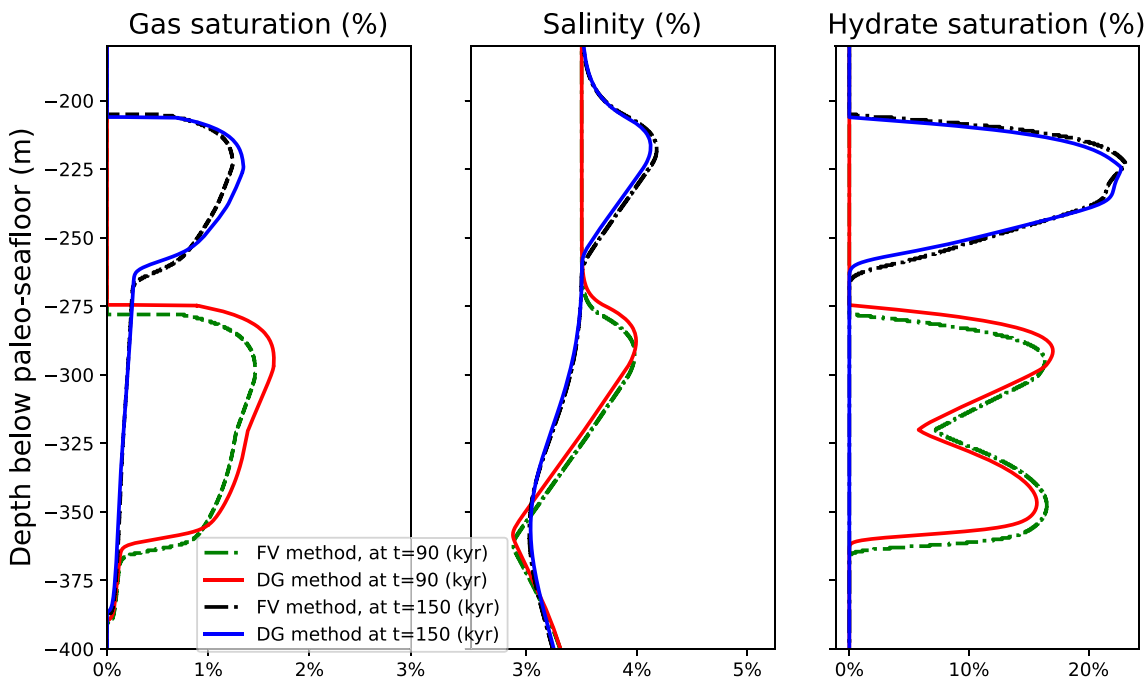

Figure 3. Validation of our scheme with finite volume (FV) method from Gupta et al. (2020). Methane hydrate recycling process at $t = 90$ and $t = 150$ Kyr for Example 1. The small difference between the FV and discontinuous Galerkin (DG) solutions arises due to propagation of the numerical error regarding lower order FV approximation.

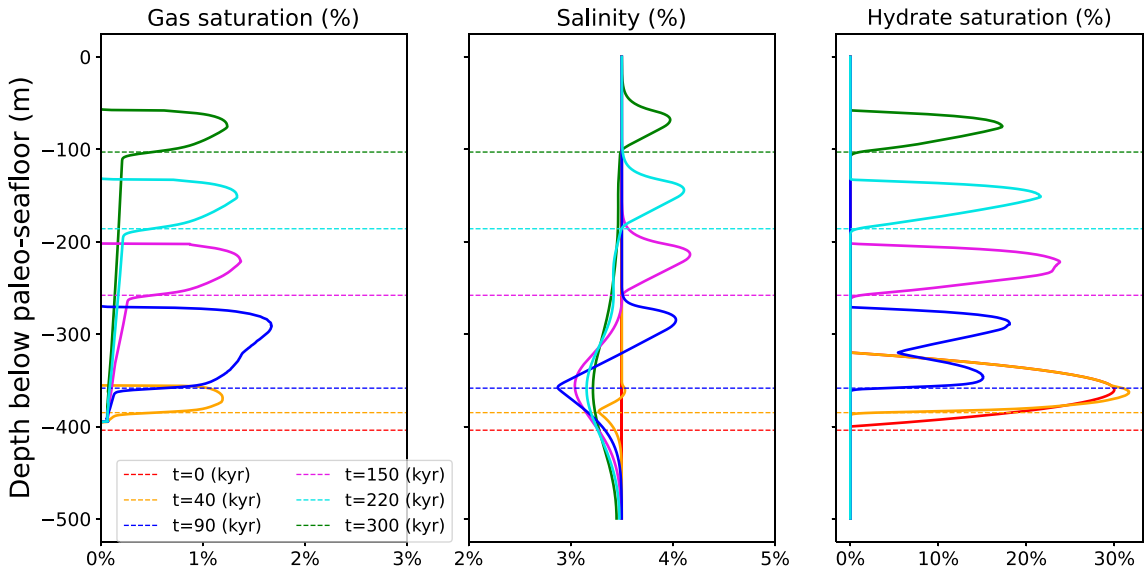

Figure 4. Methane hydrate recycling process from $t = 0$ to 300 Kyr for Example 1. The horizontal dashed lines show the base of gas hydrate stability zone (GHSZ). $q = 2$, $h = 0.5$(m).

upwards and destabilize the overlying gas hydrate layer. As gas hydrates melt, methane is released, which in sufficiently high quantity can lead to a free-gas phase to form and accumulate at the base of the gas hydrate layer. Schmidt et al. (2022) have shown that gas migration through the GHSZ in this scenario is highly dynamic and occurs in cycles. The gas hydrate layer acts as a converging-diverging nozzle in the path of upward migrating free gas, Figure 5. To be consistent with the mathematical model, in Problem 1 we consider sedimentation time period of 300 ka from $t = 0$ to $t = 300$ Kyr where $t = 0$ corresponds to the 300 ka BP.

In Figure 3, to validate our scheme, we compare our results with the Example 1 from Gupta et al. (2020). Snapshots of methane hydrate, gas saturation, and salinity at $t = 90$, 150 Kyr for both FV scheme (Gupta et al., 2020), and our DG scheme are plotted.

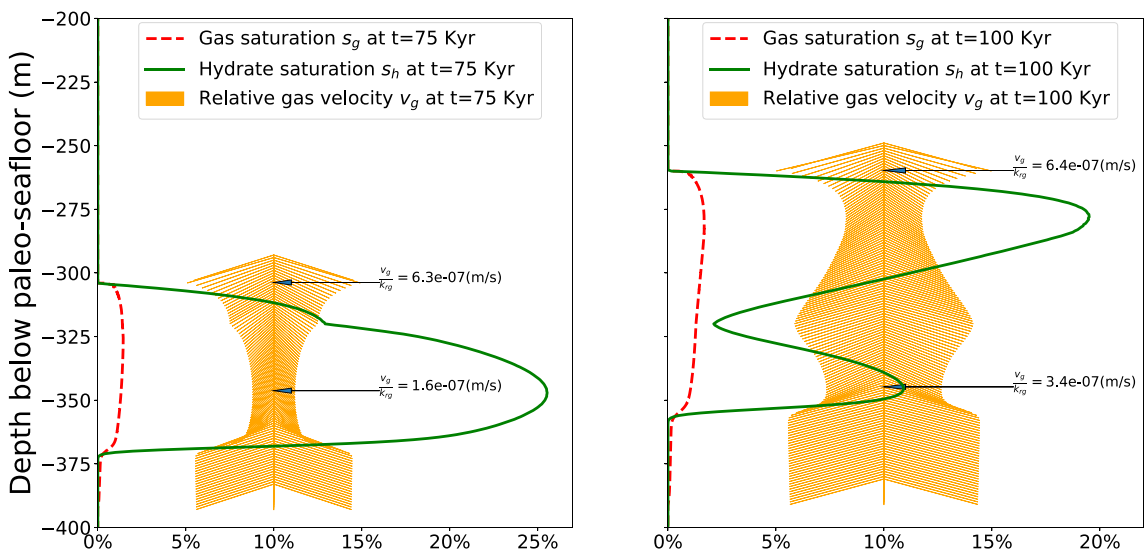

Figure 5. Nozzle effect of the hydrate layer. Gas flows upward with different velocity magnitudes due to change in the hydrate saturation. The gas velocity continuously decreases because of decreasing permeability due to increasing hydrate saturation (converging part of the hydrate nozzle). The gas velocity starts to increase when it passes the point with maximum hydrate saturation (throat of the hydrate nozzle) and it reaches its maximum velocity where the hydrate saturation is minimum (diverging part of the hydrate nozzle). Thickness of the arrows show the magnitude of the relative gas velocity.

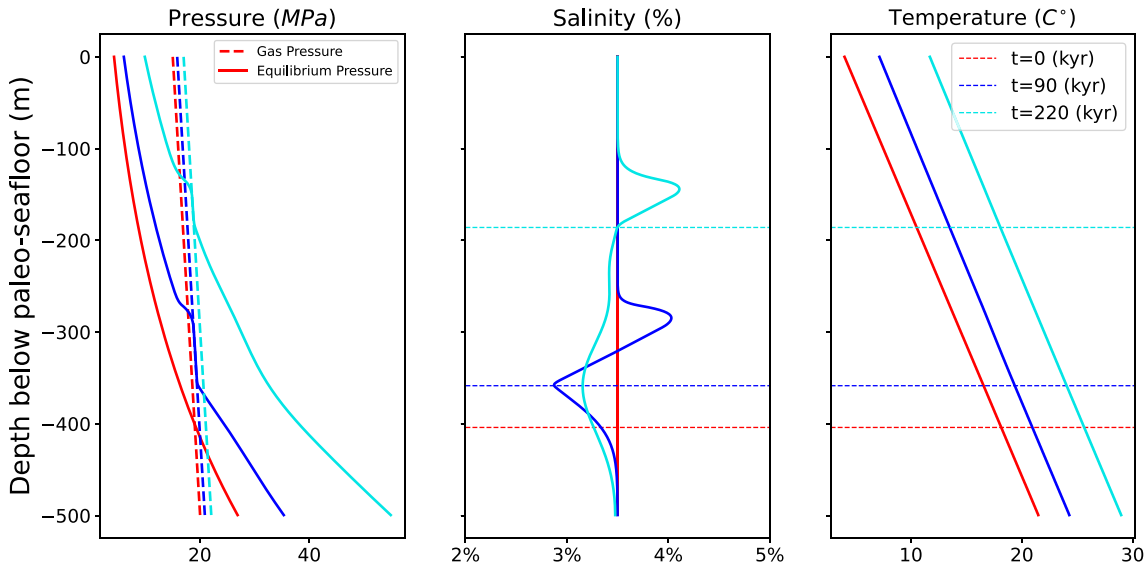

Figure 6. Upward shifting of gas hydrate stability zone (GHSZ) of Example 1. *left:* Gas pressure (dash-dot), Equilibrium pressure (solid); *middle:* Salinity; *right:* Temperature. The horizontal dashed lines show the base of GHSZ. $q = 2$, $h = 0.5$(m). The plot shows the global effect of pressure and temperature gradients on the equilibrium pressure, while salinity has a local effect on the equilibrium pressure.

Table 1
Initial and Boundary Conditions for Example 1, $d_z T_G = 35°$ C/km Denotes the Regional Geothermal Temperature Gradient (Rate of Change of Temperature (T) With Respect to Depth z), $v_{s,z} = 1$ mm/year Denotes the Sedimentation Rate

Initial conditions $t = 0$	
$\Omega = [-500, 0]$	$p_w = 15\ \text{MPa} + \rho_w \mathbf{g}(z_{sf} - z)$
	$T = 4°C + d_z T_G (z_{sf} - z)$
	$s_g = 0$
	$\chi_w^c = 0.0096$
	$\chi_w^M = 0$
	$\chi_g^H = \chi_{g,sat}^H (p_g, T)$
$-400\ \text{m} \le z \le -320\ \text{m}$	$s_h = 1.2 \left(\frac{z+320}{-400+320}\right)\left(\frac{z+400}{-320+400}\right)$
$-400\ \text{m} \ge z$ *or* $z \ge -320\ \text{m}$	$s_h = 0$
Boundary conditions $t > 0$	
$z = z_{sf}$	$p_w = 15\ \text{MPa} + \rho_w \mathbf{g} v_{s,z}(t_n + \Delta t)$
	$T = 4°C + d_z T_G v_{s,z}(t_n + \Delta t)$
	$s_g = 0$
	$\chi_w^c = \chi_w^c\|_{t=0}$
$z = -500$	$\mathbf{v}_w = 0$
	$\mathbf{v}_g = 0$
	$\nabla \chi_w^c = 0$
	$\partial_z T = d_z T_G$

Note. Initial salt mole fraction in aqueous phase is 0.0096, therefore, water salinity is 3.5%. We assume that initially there is no gas in our simulation domain, $s_g = 0$, and dissolved methane $\chi_w^M = 0$. Moreover, hydrate layer lies between depth of 320 and 400 (m) with maximum saturation of 30%. Water mole fraction in gaseous phase is then determined by VLE equation.

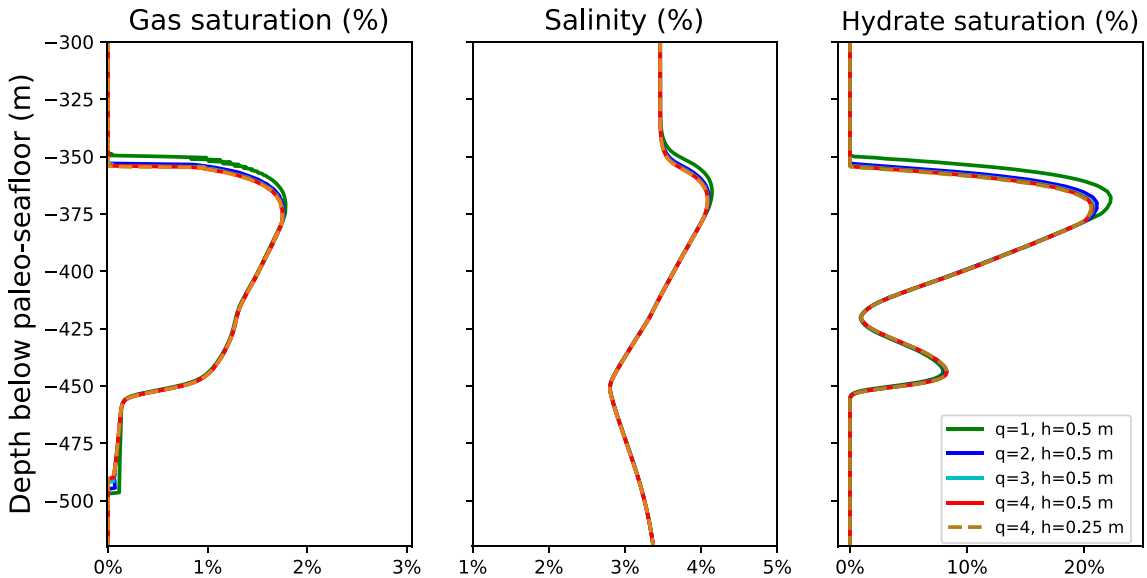

Figure 7. Linear to forth order approximation of the solution of Example 1, $t = 100$ (Kyr). The reference solution obtained on a fine mesh, $h = 0.25$ (m) with order $q = 4$ is plotted with the dashed line. The plot shows that the solution converges by increasing the order, (q), of the approximation.

In Figure 4, snapshots of methane hydrate dissociation, gas migration, hydrate reformation is shown from 300 ka BP to present day. The process of gas migration through GHSZ and MHR can be summarized as follows: Free gas phase appears below the melting gas hydrate layer and flows upwards due to buoyancy. However, as the gas flows through the hydrate layer, the gas velocity continuously decreases because of decreasing permeability due to increasing hydrate saturation (converging part of the hydrate nozzle, see Figure 5). Once the gas phase passes the point with maximum hydrate saturation s_h (throat of the hydrate nozzle, see Figure 5), the gas velocity starts to increase (diverging part of the hydrate nozzle, see Figure 5). As gas escapes the hydrate layer into the overlying GHSZ, reformation of methane hydrate occurs. The new hydrate layer continuously grows consuming the free gas provided by the dissociation of the previous methane hydrate layer, as shown in Figure 4.

While the increase of temperature by the geothermal gradient has a global effect on the equilibrium pressure, salinity has a local effect on the equilibrium pressure. This is due to the fact that heat diffuses much faster than salt (see Figure 6).

Figure 7 shows linear to fourth order approximation of the solution of Example 1. The reference solution obtained on a fine mesh, $h = 0.25$ (m) with order $q = 4$ is plotted with the dashed line. To reduce the spurious oscillations in the gas saturation, we implemented a linear polynomial reconstruction (slope limiter) for the gas saturation based on the weighted mean derivatives of the solution in the neighboring elements (Frerichs & John, 2021). After convergence of Newton method at each time step, we restrict the slope of the approximated solution. If the absolute value of the slope of the approximated solution is bigger than the numerical central difference of the neighboring cell averages. then the approximated solution will be replaced by linear approximation based on neighboring cell averages, Figure 8a. In Figure 8a, snapshot of gas saturation is plotted for $h = 0.5$ and $q = 1$ at $t = 100$ Kyr with and without slope limiter. We chose $t = 100$ Kyr, because as it is shown in Figure 4, the maximum gas saturation occurs around $t = 100$ Kyr and the escaping of gas from hydrate layer leads to oscillatory sharp front. It shows that sharp gradients of gas saturation are avoided by implementing the slope limiter.

In Figure 9, the convergence behavior of the nonlinear solver for a mesh with $h = 0.125$(m) is shown. Time step sizes drop when gas phase appears. However, they mostly remain bigger than 10 years, while in (Gupta et al., 2020) Figure 4b, Gupta et al., compared the time step size of NCP and PVS approaches which showed that even for the coarser mesh, that is, $h = 0.3125$(m), the maximum time step size of 10 years was scarcely achieved.

Example 2. *2D scenario: Gas flow through GHSZ with heterogeneous material property*

Here, we extend the above 1D scenario by introducing an anomalous material layer with high-permeability and large anisotropy within the paleo GHSZ. In the geological setting these layers represent pipe or chimney like

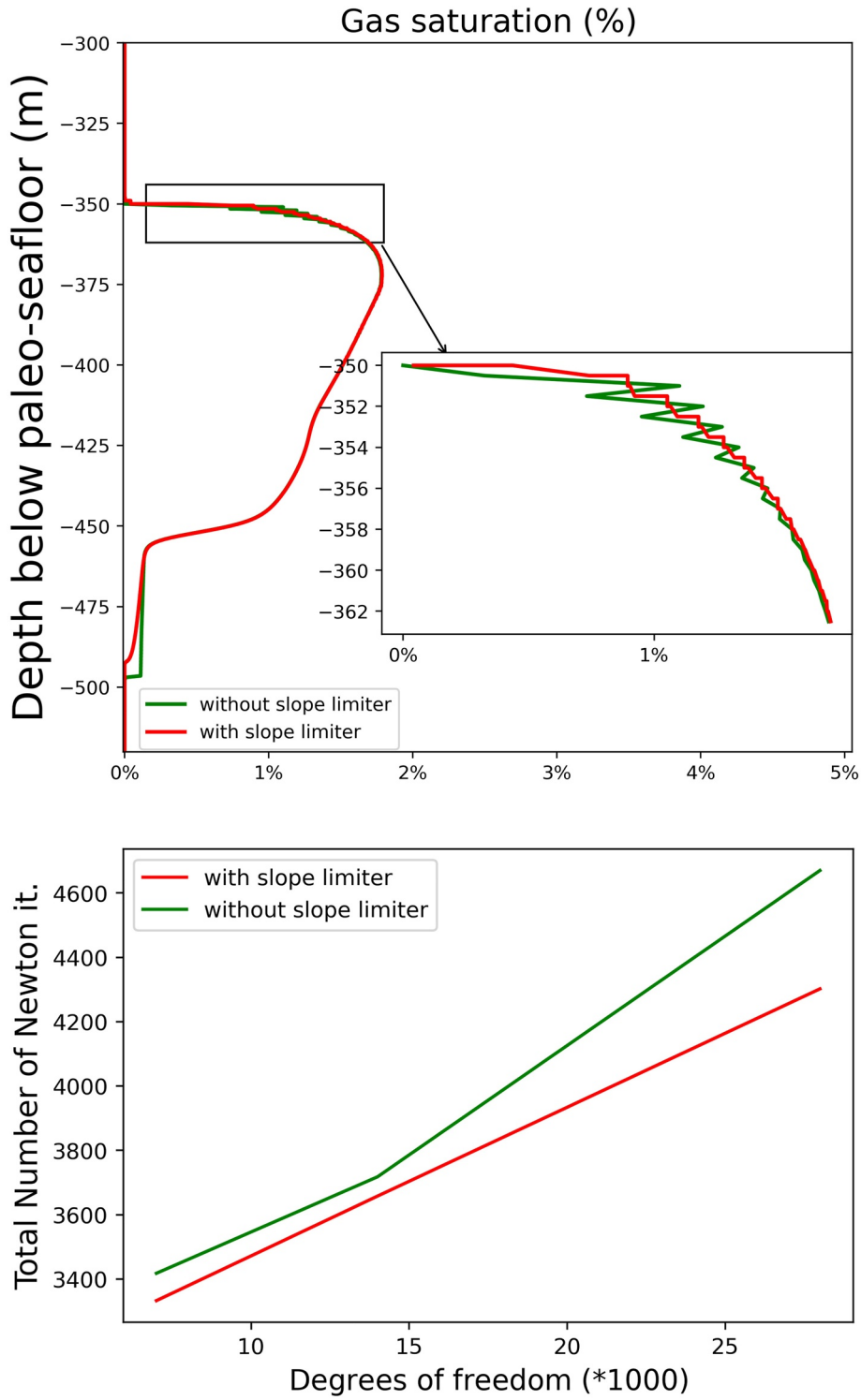

Figure 8. Impact of slope limiter on the performance of our scheme. Slope limiter, from Frerichs and John (2021), implemented for gas saturation for the solution of Example 1, $t = 100$ (Kyr), $q = 1$, $h = 0.5$(m). For different degrees of freedom, Total number of Newton iterations is plotted for Example 1 both with the slope limiter and without the slope limiter. The plot shows that the slope limiter prevents our solution to have spurious oscillations which provides physically correct approximations of the solution and therefore reduces by almost 10% the number of Newton iterations to converge.

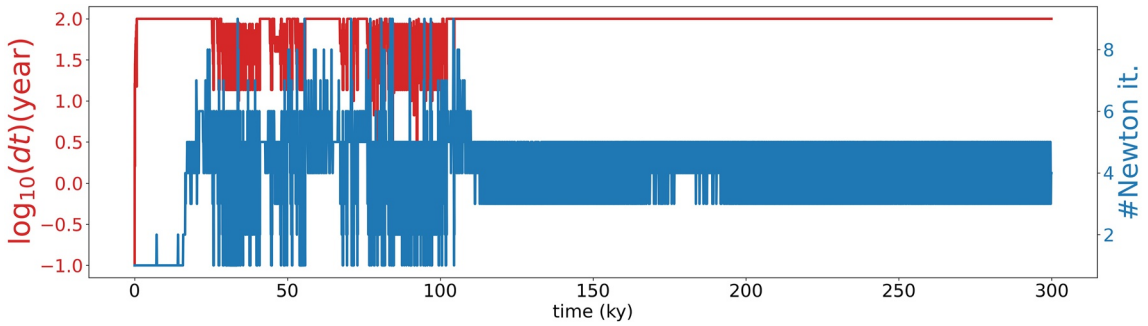

Figure 9. Numerical results for Example 1, the evolution of the time-step size during the simulation, $q = 1$, $h = 0.125$(m). Time step sizes drop when gas phase appears, however, they mostly remain bigger than 10 years.

structure with bericciated sediment or anomalous sand lenz. We consider homogeneous sediment for background material to highlight the effect of the existence of such anomalies on the MHR process. The problem schematic is shown in Figure 10, and the initial and boundary conditions are similar to Example 1 and for completeness are given in Table 2. Two different configurations are considered for the permeability tensors of the anomalous material layer, as shown in Figure 10, where $\mathbf{K}_2$ is permeability tensor of the anomalous layer that is rotation of background permeability tensor $\mathbf{K}_1$ with θ degree and scaled by K_F.

$$\mathbf{K}_1 = \begin{bmatrix} K_0 & 0 \\ 0 & K_0 \end{bmatrix}, \quad \mathbf{K}_2 = \begin{bmatrix} \cos(\theta) & -\sin(\theta) \\ \sin(\theta) & \cos(\theta) \end{bmatrix} \begin{bmatrix} K_F K_0 & 0 \\ 0 & K_F K_0, \end{bmatrix} \tag{28}$$

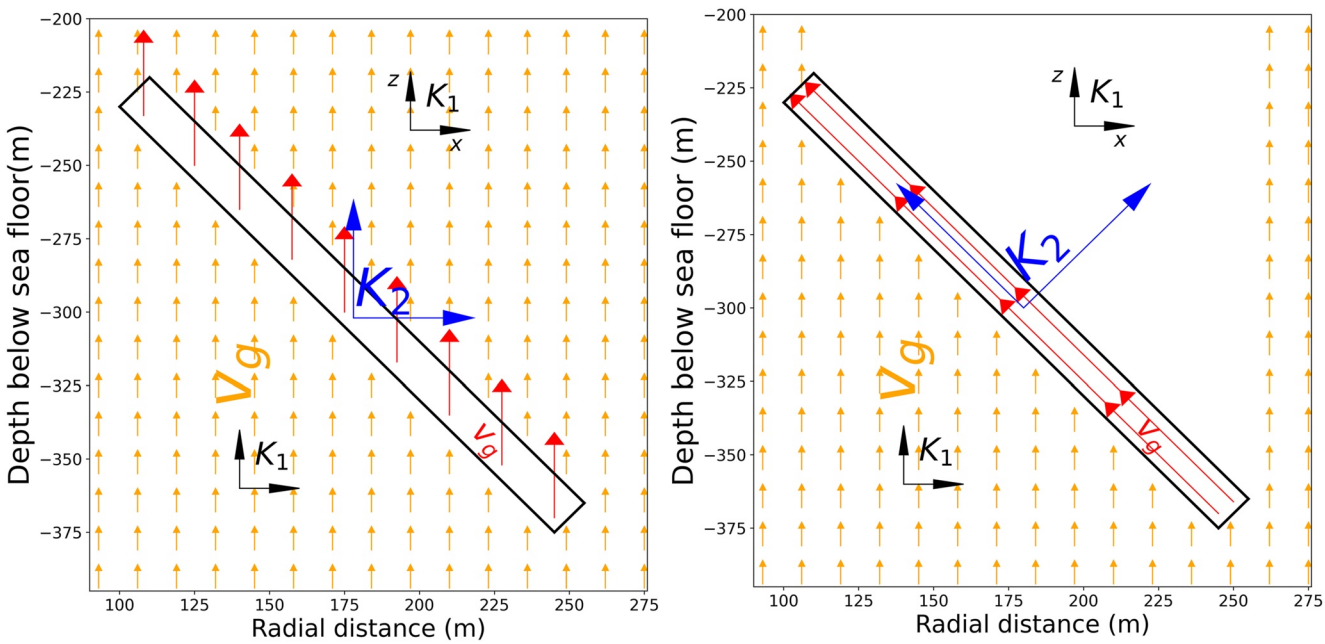

(a) Heterogeneous domain, $\theta = 0°$ (b) Heterogeneous domain, $\theta = 45°$

Figure 10. Schematic setting of Example 2 showing the anomalous anisotropic layer. v_g is the gas velocity, $\mathbf{K}_1$ is the background permeability tensor and $\mathbf{K}_2$ is the permeability tensor of the anomalous layer. In the geological setting these layers represent pipe or chimney like structure with bericciated sediment or anomalous sand lenz. Note that for both cases, we consider the scaling factor, K_F, to be 100, that is, the anomalous anisotropic layer is 100 times more permeable than the background sediment.

Table 2
Initial and Boundary Conditions for Both Configurations Case-1 and Case-2 of Example 2, With Regional Thermal Gradient $d_zT_G = 35°$ C/km and Burial Velocity $v_{s,z} = 1$ mm/year

Initial conditions $t = 0$	
$\Omega = [0, 400] \times [-500, 0]$	$p_w = 15\ \text{MPa} + \rho_w \mathbf{g}\,(z_{sf} - z)$
	$T = 2.2°C + d_zT_G\,(z_{sf} - z)$
	$s_g = 0$
	$\chi_w^c = 0.0096$
	$\chi_w^M = 0$
	$\chi_g^H = \chi_{g,sat}^H\,(p_g, T)$
$-460\ \text{m} \le z \le -380\ \text{m}$	$s_h = 1.2\left(\frac{z+380}{-460+320}\right)\left(\frac{z+460}{-380+460}\right)$
$-460\ \text{m} \ge z\ or\ z \ge -380\ \text{m}$	$s_h = 0$
Boundary conditions $x \in \partial\Omega$, $t > 0$	
$z = z_{sf}$	$p_w = 15\ \text{MPa} + \rho_w \mathbf{g} v_{s,z}\,(t_n + \Delta t)$
	$T = 2.2°C + d_zT_G v_{s,z}\,(t_n + \Delta t)$
	$s_g = 0$
	$\chi_w^c = \chi_w^c\vert_{t=0}$
	$\mathbf{v}_w = 0$
$x = 0\ or\ x = 400\ or\ z = -500$	$\mathbf{v}_g = 0$
	$\nabla \chi_w^c = 0$
$z = -500$	$\partial_z T = d_zT_G$

K_0 is the absolute scalar permeability of the background sediment and K_F is a scaling factor for the absolute permeability of the anomalous layer.

In the first configuration, the degree of rotation is 0°. This is the simplest form of anisotropy, and the only form that can be handled by our finite volume based numerical solver with linear two-point flux approximations. This form, however, ignores the strongly directional properties of such a layer (e.g., flow through fractures). The second configuration accounts for this by rotating the permeability tensor along the layer axis. Such form of anisotropy (with full tensor) cannot be handled with a linear two-point flux approximation in a finite volume scheme, and instead, requires advanced methods like multi-point flux approximations or non-linear two-point flux approximations, both of which are computationally more expensive and conceptually more complicated. However, in DG discretization, any form of material anisotropy can be handled easily without additional overheads. The direction of the gas velocity depends on the permeability tensor of the layers, as schematically shown in Figure 10. When gas reaches the high permeable layer in case of the rotated permeability tensor, it will flow dominantly along the layer, bypassing the regions above the layer, as shown in Figure 10b.

Figure 11 shows snapshots of the MHR and gas migration processes for configuration with $\theta = 0°$, and Figure 12 shows snapshots for the configuration with $\theta = 45°$. Notice how in the former, *more* gas is transported to the region above the anomalous layer and a thicker hydrate layer with higher saturation develops, while in the latter, gas is completely diverted through the anomalous layer, and the gas migration through the GHSZ is fully localized within a focused flow channel that looks strikingly similar to the chimney-like fluid escape structures observed in seimic profiles, see (Crutchley et al., 2021; Waage et al., 2019). Notice also that the gas ascent toward the sea floor is much faster in the latter configuration compared to the former. What is especially interesting is that even though the anomalous layer has the same geometry and same heterogeneity in both configurations, the gas migration shows completely different behavior due to the nature of the anisotropy. These idealized scenarios clearly demonstrate how the approximation of the properties of the complex sediment structures can lead to remarkably large deviations in the system dynamics.

In fact, the development of focused gas flow in Figure 12c is a particularly interesting result with direct implications for real world scenarios. For example, seismic data of the gas hydrate system in New Zealand's southern Hikurangi subduction margin shows a network of normal faults lying within the GHSZ (Crutchley et al., 2021). Data shows a broad zone of both negative- and positive-polarity reflections (interpreted as sediment layer with coexisting free gas and gas hydrate). This zone lies directly beneath sub-vertical gas-flow conduits (possibly a combination of gas-charged normal fault and gas pipe/chimney), and extends up to the base of the regional GHSZ. In their analysis of this data, Crutchley et al. (2021) highlight the importance of considering the structural heterogeneity within GHSZ and in particular, the impact of normal faults on the gas migration through the GHSZ. Similarly, high resolution 3D seismic data from the Storfjordrenna gas hydrate pingos field in northwestern Barents Sea shows that the pingos lie on top of gas chimneys that are connected to inclined faults within the underlying free gas and hydrate?bearing sedimentary rocks (Waage et al., 2019), highlighting once again the relationship between gas hydrate dynamics and regional fault system. Our numerical scheme capture this dynamics quite well and results illustrate the role of structural heterogeneity on dynamics of gas hydrates and gas migration through GHSZ. Moreover, our results emphasize the dramatic deviations that can appear in simulated system behavior if the structural heterogeneities are not appropriately handled.

5. Conclusion

Natural gas hydrate systems are characterized by strongly coupled and highly dynamic multiphysics interactions that require sophisticated numerical schemes to capture the system behavior accurately and robustly. A particular challenge is related to the complex structure of the geological subsurface. Classically, problems like burial driven

Table 3
Hydrate and Material Properties

Property	Ex. 1	Ex. 2
Hydrate		
Density ρ_h (kg/m^3)	920	
Hydration number N_h	5.90	
Thermal conductivity k_h^{th} (W/m/K)	0.5	
Specific heat capacity Cp_h (J/kg/K)	2,327	$(1.937\,T^3 - 1.5151\,T^2 + 3.9554\,T - 342.7) \times 10^3$
Salt		
Diffusion coeffiecient D_w^c (m^2/s)	10^{-9}	
Soil		
Density ρ_s (kg/m^3)	2,600	
Thermal conductivity k_s^{th} (W/m/K)	3.0	
Specific heat capacity Cp_s (J/kg/K)	1,000	
Hydrate phase change kinetics		
Hydrate equilibrium pressure P_e (Pa)		$\exp\left(38.592 - \frac{8533.8}{T} + 4.4824\chi_w^c\right)$
Kinetic rate constant k^r (mol/m^2/Pa/s)	10^{-17}	
Specific surface area A_0 (m^2/m^3)	10^5	
Heat of reaction $\dot{Q}_h$ (W/m^3)		$\frac{\dot{g}_h}{M_h}(a_1 + a_2 T)$ where $a_1 = 56{,}599$, $a_2 = -16.744$
Hydrulic propertoes		
Absolute intrinsic permeability $\mathbf{K}_0$ (m^2)	10^{-15}	10^{-15}, 10^{-13}
Total porosity ϕ	0.5	
Brooks-Corey parameters P_0 (Pa), λ	5×10^4,	1.2
Sphericity parameter m	1	
Residual saturations S_{wr}, S_{gr}	0.0	

recycling are studied in homogeneous sediments, or sediments with a layered stratigraphy that follows the paleo and present sea floor topographies. Existence of strongly anisotropic anomalous layers with large contrasts in properties within the gas hydrate stability zone can lead to significant deviations in the system dynamics. An accurate prediction of these deviations is critical for estimating the present day geological carbon repositories, response of hydrate-bearing sediments to changing environmental and climate stressors, and their geomechanical stability in response to natural and anthropogenic activities. In this manuscript, we present a new numerical scheme based on the DG method for our methane hydrate model (Gupta et al., 2020). The motivation for the development of this new numerical scheme was to enhance the flexibility compared to FV approaches so that we can handle the structural complexities of the sediments more accurately, and therefore, be able to consider more realistic geological settings. The choice of the DG scheme was specifically inspired by the fact that it is locally mass conservative (like the finite volume method on which our earlier simulators are based), and can approximate the fluxes in anisotropic fields more generally without additional overheads (like larger stencils that are needed for extending finite volume schemes with methods like multi-point and nonlinear two-point flux approximations in order to capture material anisotropy). Here we show that (a) the semi-smooth Newton solver for handling gas-water phase transitions performs well with a DG based discretization, (b) the presented DG scheme is able to capture the multiphysics dynamics of the methane hydrate systems accurately, and (c) the presented DG scheme is able to accurately capture the gas migration and hydrate recycling processes through strongly anisotropic materials. We also demonstrate that layer properties influence sensitively the numerical simulation results and incomplete knowledge can result in very large prediction errors of the recycling process.

Journal of Geophysical Research: Solid Earth

10.1029/2022JB025592

Table 4
Water and Methane Properties

Property	Ex. 1	Ex. 2
Water		
Density ρ_w (kg/m^3)	1030.21	$1027 + 0.45 p_w[MPa] - 0.15(T[°C] - 10) + 352.1\,(\chi_w^c - 0.0096)$
Dynamic viscosity μ_w (*Pa*.s)	0.00136	$1.792 \times 10^{-3} \exp\left(-1.94 - 4.8\left(\frac{273.15}{T}\right) + 6.75\left(\frac{273.15}{T}\right)^2\right)$
Thermal conductivity k_w^{th} (*W*/m/*K*)	0.59	$0.57153\left(1 + 0.003\,(T\ [°C] - 10.25\left(\frac{T[°C]}{1000}\right)^2 - 0.0797\chi_w^c + 0.653 p_w[GPa]\right)$
Specific heat capacity Cp_w (*J*/*kg*/*K*)		3,945
Saturation vapor pressure P_{sat}^H (*Pa*)		$P_c \exp\left(\frac{1}{T_r}\left(c_1(1-T_r) + c_2(1-T_r)^{1.5} + c_3(1-T_r)^3 + c_4(1-T_r)^{3.5} + c_5(1-T_r)^4 + c_6\ (1-T_r)^{7.5}\right)\right)$
		$P_c = 22.064\,MPa,\ T_c = 647.096K,\ T_r = \frac{T}{T_c},\ c_1 = -7.85951783,\ c_2 = 1.84408259$
		$c_3 = -11.7,866,497,\ c_4 = 22.6,807,411,\ c_5 = -15.9,618,719,\ c_6 = 1.80,122,502$
Diffusion coefficient D_g^H (m^2/s)	$6.38\ 10^{-7}$	$2.26\ 10^{-9}\,T + \frac{0.002554}{p_g}$
Methane		
Density ρ_g (kg/m^3)	$0.002756\frac{p_g}{T}\frac{p_g}{z^M R^M T}$	
	where, $R^M = \frac{8314.462175}{16.04}$, and z^M is estimated using Peng Robinson EoS	
Dynamic viscosity μ_g (*Pa*.s)	$1.4055\ 10^{-5}$ $\mu_0\left(\frac{273.15+162}{T+162}\right)\left(\frac{T}{273.15}\right)^{1.5}$	
	where $\mu_0 = 1.0707 \times 10^{-5} - 4.8134 \times 10^{-14} p_g - 4.1719 \times 10^{-21} p_g^2 + 7.3232 \times 10^{-28} p_g^3$	
Thermal conductivity k_g^{th} (W/m/K)	0.03121	$-8.863 \times 10^{-3} + 2.42 \times 10^{-4} T - 6.997 \times 10^{-7}\,T^2 + 1.225 \times 10^{-9}\,T^3$
Specific heat capacity Cp_g (*J*/*kg*/*K*)	2,168.65	$1{,}238 + 3.13\,T + 7.9057 \times 10^{-4}\,T^2 - 6.858 \times 10^{-7}\,T^3$
Saturation vapor pressure H_w^M (*MPa*)	1.343×10^5 $\exp\left(\log\left(P_{sat}^H\right) - \frac{b_0 + b_1(1-T_r)^{0.355}}{T_r} + b_2 \exp(1-T_r)\,T_r^{-0.41}\right)$	
	where $b_0 = 11.0094,\ b_1 = -4.8362,\ b_2 = 12.522$	
Diffusion coefficient D_w^M (m^2/s)	1.57×10^{-11} $1.57 \times 10^{-11}\left(\frac{p_w}{1.0135 \times 10^5}\right)\exp\left(-\frac{0.003475}{T}\right)$	

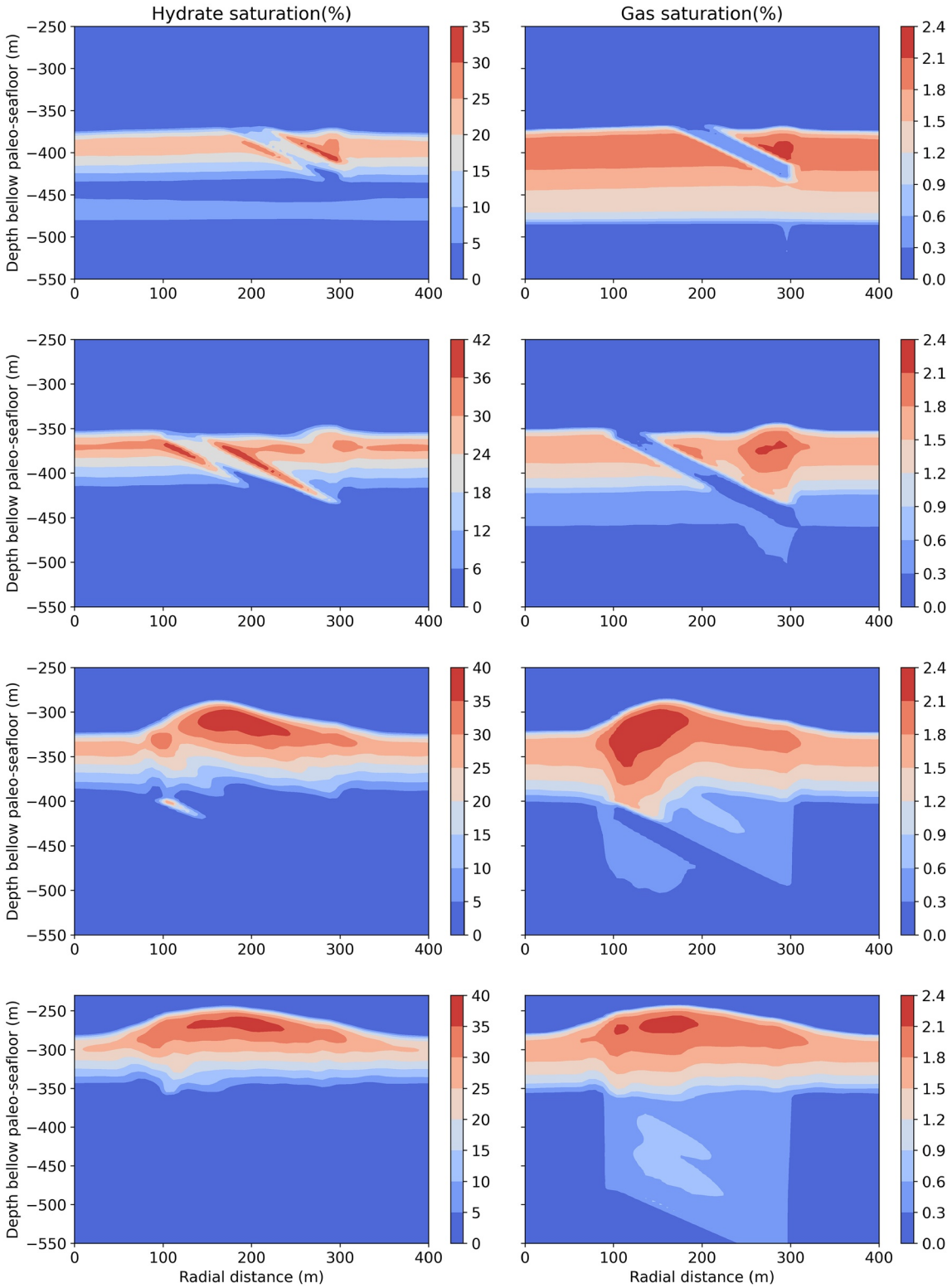

Figure 11. Numerical results for case-1 of Example 2. The figure shows snapshots of (from left to right): s_h, s_g within the domain of interest $\Omega = [0, 400] \times [-500, 0]$ at different times. (a) $t = 65$ Kyr (235 ka BP), (b) $t = 75$ Kyr (225 ka BP), (c) $t = 85$ Kyr (215 ka BP), (d) $t = 90$ Kyr (210 ka BP).

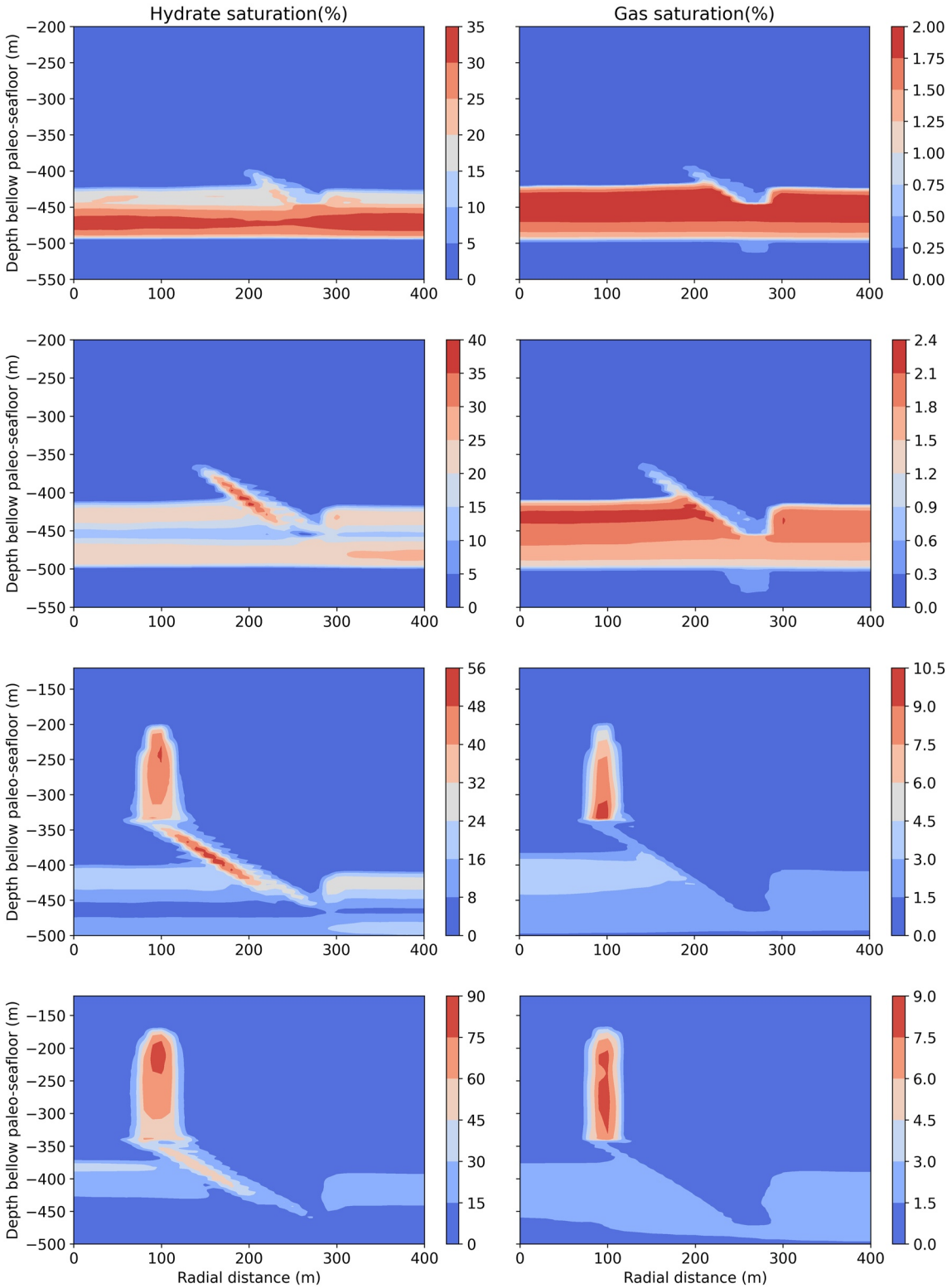

Figure 12. Numerical results for case-2 of Example 2 with one heterogeneous layer. The figure shows snapshots of (from left to right): s_h, s_g within the domain of interest $\Omega = [0, 400] \times [-500, 0]$ at different times. Strong anisotropy leads to development of focused gas flow. (a) t = 65 Kyr (235 ka BP), (b) t = 75 Kyr (225 ka BP), (c) t = 85 Kyr (215 ka BP), (d) t = 90 Kyr (210 ka BP).

Appendix A: Discontinuous Galerkin Method

In this section we present a discontinuous finite element method for Problem 1. In the following, all functions and parameters are assumed to be non-dimensional. The domain, $\Omega \subset \mathbb{R}^d$, will be partitioned into quadrilateral elements $\Omega_l \in \mathcal{T}_h$ where $\mathcal{T}_h$ is a mesh of the domain and $l = 1 \dots |\mathcal{T}_h|$. Broken Sobolev spaces and Bochner spaces can therefore be written as

$$\begin{aligned} \mathcal{H}^1(\Omega, \mathcal{T}_h) &= \left\{ v \in L^2(\Omega) \;\middle|\; v|_{\Omega_l} \in \mathcal{H}^1(\Omega_l), \;\; \forall \Omega_l \in \mathcal{T}_h \right\}, \\ \mathcal{H}^1_b(\Omega, \mathcal{T}_h) &= \left\{ v \in \mathcal{H}^1(\Omega, \mathcal{T}_h) \;\middle|\; 0 \le v \le 1 \quad a.e. \text{ in } \Omega \right\}, \\ \mathcal{C}\left(\mathbb{T}; \mathcal{H}^1(\Omega, \mathcal{T}_h)\right) &= \left\{ v : \mathbb{T} \to \mathcal{H}^1(\Omega, \mathcal{T}_h) \;\middle|\; v \text{ is continuous} \right\}. \end{aligned} \tag{A1}$$

F is called an interior interface if $|F| \neq 0$ and there exist Ω_F^- and Ω_F^+ in $\mathcal{T}_h$, see Figure A1, such that $F \subseteq \Omega_F^- \cap \Omega_F^+$. $\mathbf{n}_F$ is the unit normal vector to the interface F and the direction is arbitrary but fix. Let $\mathcal{F}^I$ be the set of all interior interfaces. Similarly, let $\mathcal{F}^B = \mathcal{F}^D \cup \mathcal{F}^N$ be the set of all the boundary faces including Dirichlet $\mathcal{F}^D$ and Neumann $\mathcal{F}^N$ boundary faces. Let $F \in \mathcal{F}^I$ and $F \subseteq \Omega_F^- \cap \Omega_F^+$ then $\forall v \in \mathcal{H}^1(\Omega\mathcal{T}_h)$, we introduce

$$\begin{aligned} v_F^- &= v|_{\Omega_F^-}, & v_F^+ &= v|_{\Omega_F^+} \\ \{v\}_F &= \frac{1}{2}\left(v_F^- + v_F^+\right), & [v]_F &= v_F^- - v_F^+ \end{aligned} \tag{A2}$$

Moreover, the definitions for all boundary faces has to be adopted in a proper way. In the following, we consider flux continuity on the interfaces, that is,

$$[\nabla v]_F . \mathbf{n}_F = 0, \tag{A3}$$

therefore, $\forall F \in \mathcal{F}^I$ and $\forall u, v \in \mathcal{H}^1(\Omega\mathcal{T}_h)$, we have

$$\mathbf{n}_F . \nabla u_F^- \, v_F^- - \mathbf{n}_F . \nabla u_F^+ \, v_F^+ = \mathbf{n}_F . \{\nabla u\}_F \, [v]_F + \mathbf{n}_F . [\nabla u]_F \, \{v\}_F = \mathbf{n}_F . \{\nabla u\}_F \, [v]_F. \tag{A4}$$

Let $\mathcal{V} = \mathcal{C}\left(\mathbb{T}; \mathcal{H}^1(\Omega, \mathcal{T}_h)\right)$ be the Bochner space for p_w, T and $\mathcal{V}_b = \mathcal{C}\left(\mathbb{T}; \mathcal{H}^1_b(\Omega, \mathcal{T}_h)\right)$ be the Bochner space for $s_g, s_h, \chi_w^M, \chi_g^H, \chi_w^c$, then $\forall i \in C$, we consider the following functionals to define variational formulation for Problem 1,

$$\begin{aligned} b^i &: \mathcal{V}^2 \times \mathcal{V}_b^5 \times \mathcal{H}^1(\Omega, \mathcal{T}_h) \to \mathbb{R}, \\ a^i &: \mathcal{V}^2 \times \mathcal{V}_b^5 \times \mathcal{H}^1(\Omega, \mathcal{T}_h) \to \mathbb{R}, \\ a^{\sigma i} &: \mathcal{V}^2 \times \mathcal{V}_b^5 \times \mathcal{H}^1(\Omega, \mathcal{T}_h) \to \mathbb{R}, \\ l^i &: \mathcal{V}^2 \times \mathcal{V}_b^5 \times \mathcal{H}^1(\Omega, \mathcal{T}_h) \to \mathbb{R}, \end{aligned} \tag{A5}$$

Thus, variational formulation for Problem 1 can be written as follows

Problem 2. *(Variational Formula) Find* $\mathbf{U} \in \mathcal{V}^2 \times \mathcal{V}_b^5$ such that $\forall v \in \mathcal{H}^1(\Omega, \mathcal{T}_h)$ *and* $\forall i \in C$

$$\partial_t b^i(\mathbf{U}; v) + a^i(\mathbf{U}; v) + a^{\sigma i}(\mathbf{U}; v) = l^i(\mathbf{U}; v) + a_D^{\sigma i}(\mathbf{U}; v) \tag{A6}$$

hold, where for $\kappa = M, H, c$

$$
\begin{aligned}
b^M(\mathbf{U};v) &:= \sum_{\Omega_l}\left(\phi\rho_w\,\chi_w^M\,s_w+\phi\rho_g\,\chi_g^M\,s_g,v\right)_{\Omega_l},\\
a^M(\mathbf{U};v) &:= -\sum_{\Omega_l}\left(\rho_w\chi_w^M\,\mathbf{v}_w+\rho_g\,\chi_g^M\,\mathbf{v}_g,\nabla v\right)_{\Omega_l}\\
&- \sum_{\Omega_l}\left(\phi\,s_w\,\mathbf{J}_w^M+\rho_g\,s_g\,\mathbf{J}_g^M,\nabla v\right)_{\Omega_l}\\
&+ \sum_{F\in\mathcal{F}^{I\cup D}}\left(\left\{\rho_w\,\chi_w^M\,\mathbf{v}_w+\rho_g\,\chi_g^M\,\mathbf{v}_g\right\}.\mathbf{n},[v]\right)_F\\
&\quad -\Theta\left(\left\{\rho_w\,\chi_w^M\,K\,\frac{k_{rw}}{\mu_w}\nabla v\right\}.\mathbf{n},[p_w]\right)_F\\
&+ \sum_{F\in\mathcal{F}^{I\cup D}}\left(\left\{\phi\,s_w\,\mathbf{J}_w^M+\phi\,s_g\,\mathbf{J}_g^M\right\}.\mathbf{n},[v]\right)_F\\
&+ \sum_{F\in\mathcal{F}^{N}}\left(\left(\rho_w\,\chi_w^M\,\mathbf{v}_w+\phi\,s_w\,\mathbf{J}_w^M+\rho_g\,\chi_g^M\,\mathbf{v}_g+\phi\,s_g\,\mathbf{J}_g^M\right).\mathbf{n},v\right)_F
\end{aligned}
\tag{A7}
$$

$$
\begin{aligned}
a^{\sigma M}(\mathbf{U};v) &:= \sum_{F\in\mathcal{F}^{I\cup D}}\left(\sigma_p\,[p_w],[v]\right)_F,\qquad a_D^{\sigma M}(\mathbf{U};v):=\sum_{F\in\mathcal{F}^D}\left(\sigma_p\,p_w^D,v\right)_F,\\
l^M(\mathbf{U};v) &:= \sum_{\Omega_l}\left(\dot{g}^M,v\right)_{\Omega_l},\\
&b^h(\mathbf{U};v):=\sum_{\Omega_l}\left(\phi\,\rho_h\,s_h,v\right)_{\Omega_l},\\
&a^h(\mathbf{U};v):=0,\\
&a^{\sigma h}(\mathbf{U};v):=\sum_{F\in\mathcal{F}^I}\left(\sigma_s\,[s_h],[v]\right)_F\qquad a_D^{\sigma h}(\mathbf{U};v):=0,\\
&l^h(\mathbf{U};v):=\sum_{\Omega_l}\left(\dot{g}_h,v\right)_{\Omega_l},
\end{aligned}
\tag{A8}
$$

$$
\begin{aligned}
b^H(\mathbf{U};v) &:= \sum_{\Omega_l}\left(\phi\rho_w\,\chi_w^H\,s_w+\phi\rho_g\,\chi_g^H\,s_g,v\right)_{\Omega_l},\\
a^H(\mathbf{U};v) &:= -\sum_{\Omega_l}\left(\rho_w\chi_w^H\,\mathbf{v}_w+\rho_g\,\chi_g^H\,\mathbf{v}_g,\nabla v\right)_{\Omega_l}\\
&- \sum_{\Omega_l}\left(\phi\,s_w\,\mathbf{J}_w^H+\rho_g\,s_g\,\mathbf{J}_g^H,\nabla v\right)_{\Omega_l}\\
&+ \sum_{F\in\mathcal{F}^{I\cup D}}\left(\left\{\rho_w\,\chi_w^H\,\mathbf{v}_w+\rho_g\,\chi_g^H\,\mathbf{v}_g\right\}.\mathbf{n},[v]\right)_F\\
&\quad -\Theta\left(\left\{\rho_g\,\chi_g^H\,K\,\frac{k_{rg}}{\mu_g}\nabla v\right\}.\mathbf{n},\left[s_g\right]\right)_F\\
&+ \sum_{F\in\mathcal{F}^{I\cup D}}\left(\left\{\phi\,s_w\,\mathbf{J}_w^H+\phi\,s_g\,\mathbf{J}_g^H\right\}.\mathbf{n},[v]\right)_F\\
&+ \sum_{F\in\mathcal{F}^{N}}\left(\left(\rho_w\,\chi_w^H\,\mathbf{v}_w+\phi\,s_w\,\mathbf{J}_w^H+\rho_g\,\chi_g^H\,\mathbf{v}_g+\phi\,s_g\,\mathbf{J}_g^H\right).\mathbf{n},v\right)_F,
\end{aligned}
\tag{A9}
$$

$$
\begin{aligned}
a^{\sigma H}(\mathbf{U};v) &:= \sum_{F\in\mathcal{F}^{I\cup D}}\left(\sigma_s\,\left[s_g\right],[v]\right)_F,\qquad a_D^{\sigma,H}(\mathbf{U};v):=\sum_{F\in\mathcal{F}^D}\left(\sigma_s\,s_g^D,v\right)_F,\\
l^H(\mathbf{U};v) &:= \sum_{\Omega_l}\left(\dot{g}^H,v\right)_{\Omega_l},\\
b^e(\mathbf{U};v) &:= \sum_{\Omega_l}\left((1-\phi)\,\rho_s\,u_s\,+\phi\,\left(\rho_w\,u_w\,s_w+\rho_g\,u_g\,s_g+\rho_h\,u_h\,s_h\right),v\right)_{\Omega_l},\\
a^e(\mathbf{U};v) &:= -\sum_{\Omega_l}\left(\rho_w\,h_w\,\mathbf{v}_w+\rho_g\;h_g\,\mathbf{v}_g-k_{eff}^{th}\nabla T,\nabla v\right)_{\Omega_l}\\
&+ \sum_{F\in\mathcal{F}^{I\cup D}}\left(\left\{\rho_w\,h_w\,\mathbf{v}_w+\rho_g\;h_g\,\mathbf{v}_g-k_{eff}^{th}\nabla T\right\}.\mathbf{n},[v]\right)_F\\
&\quad +\Theta\left(\left\{-k_{eff}^{th}\nabla v\right\}.\mathbf{n},[T]\right)_F\\
&+ \sum_{F\in\mathcal{F}^{N}}\left(\left(\rho_w\,h_w\,\mathbf{v}_w+\rho_g\,h_g\,\mathbf{v}_g-k_{eff}^{th}\nabla T\right).\mathbf{n},v\right)_F.\\
a^{\sigma e}(\mathbf{U};v) &:= \sum_{F\in\mathcal{F}^{I\cup D}}\left(\sigma_T\,[T],[v]\right)_F\qquad a_D^{\sigma e}(\mathbf{U};v):=\sum_{F\in\mathcal{F}^D}\left(\sigma_T\,T^D,v\right)_F,\\
l^e(\mathbf{U};v) &:= \sum_{\Omega_l}\left(\dot{Q}_h,v\right)_{\Omega_l},
\end{aligned}
\tag{A10}
$$

$$
\begin{aligned}
&b^{ncp1}(\mathbf{U};v) := 0,\\
&a^{ncp1}(\mathbf{U};v) := \sum_{\Omega_l}\left(s_g - \max\left\{0\, s_g - 1 + \chi_g^M + \chi_g^H\right\}, v\right)_{\Omega_l},\\
&a^{\sigma ncp1}(\mathbf{U};v) := \sum_{F\in\mathcal{F}^I}\left(\sigma_x\left[\chi_g^H\right],[v]\right)_F \qquad a_D^{\sigma ncp1}(\mathbf{U};v) := 0,\\
&l^{ncp1}(\mathbf{U};v) := 0,
\end{aligned}
\tag{A11}
$$

$$
\begin{aligned}
&b^{ncp2}(\mathbf{U};v) := 0,\\
&a^{ncp2}(\mathbf{U};v) := \sum_{\Omega_l}\left(s_w - \max\left\{0, s_w - 1 + \chi_w^M + \chi_w^H + \chi_w^c\right\}, v\right)_{\Omega_l},\\
&a^{\sigma ncp2}(\mathbf{U};v) := \sum_{F\in\mathcal{F}^I}\left(\sigma_x\left[\chi_w^M\right],[v]\right)_F, a_D^{\sigma,ncp2}(\mathbf{U};v) := 0,\\
&l^{ncp2}(\mathbf{U};v) := 0,
\end{aligned}
\tag{A12}
$$

$$
\begin{aligned}
b^c(\mathbf{U};v) \;&:=\; \sum_{\Omega_l}(\phi\rho_w\,\chi_w^c s_w, v)_{\Omega_l},\\
a^c(\mathbf{U};v) \;&:=\; -\sum_{\Omega_l}(\rho_w\chi_w^c\,\mathbf{v}_w + \phi\, s_w\,\mathbf{J}_w^c, \nabla v)_{\Omega_l}\\
&\quad + \sum_{F\in\mathcal{F}^{I\cup D}}(\{\rho_w\,\chi_w^c\,\mathbf{v}_w + \phi\, s_w\,\mathbf{J}_w^c\}.\mathbf{n}, [v])_F\\
&\quad - \Theta\left(\{\phi\, s_w\,\tau\mathbf{D}_w^c\rho_w\nabla v\}.\mathbf{n}, \left[\chi_w^c\right]\right)_F\\
&\quad + \sum_{F\in\mathcal{F}^N}((\rho_w\,\chi_w^c\,\mathbf{v}_w + \phi\, s_w\,\mathbf{J}_w^\kappa).\mathbf{n}, v)_F\\
a^{\sigma c}(\mathbf{U};v) \;&:=\; \sum_{F\in\mathcal{F}^{I\cup D}}\left(\sigma_x\left[\chi_w^c\right],[v]\right)_F \qquad a_D^{\sigma c}(\mathbf{U};v) := \sum_{F\in\mathcal{F}^D}\left(\sigma_x\,\chi_w^{cD}, v\right)_F,\\
l^c(\mathbf{U};v) \;&:=\; \sum_{\Omega_l}(\dot{g}^c, v)_{\Omega_l},
\end{aligned}
\tag{A13}
$$

and σ_s, σ_p, σ_x, σ_T are the positive penalty coefficients corresponding to the saturation, pressure, mole fraction and temperature functions respectively, $\Theta = 1, -1, 0$ in the cases of symmetric, nonsymmetric and incomplete forms of variational formulation for Problem 1.

We introduce the following vector notations:

$$
\begin{aligned}
b(\mathbf{U};v) &= \left[\; b^i(\mathbf{U};v)\;\right]_{i\in C} \qquad & a(\mathbf{U};v) &= \left[\; a^i(\mathbf{U};v)\;\right]_{i\in C}\\
l(\mathbf{U};v) &= \left[\; l^i(\mathbf{U};v)\;\right]_{i\in C} \qquad & a^\sigma(\mathbf{U};v) &= \left[\; a^{\sigma i}(\mathbf{U};v)\;\right]_{i\in C} \quad a_D^\sigma(\mathbf{U};v) = \left[\; a_D^{\sigma i}(\mathbf{U};v)\;\right]_{i\in C}
\end{aligned}
\tag{A14}
$$

Let $q_i \geq 0$ be an integer for every $i \in C$. We consider the finite-dimensional subspace of broken Sobolev spaces (Equation A1)

$$
\begin{aligned}
S_h^{q_i} &= \left\{ v \in L^2(\Omega) \;\middle|\; v|_{\Omega_l} \in \mathbb{P}^{q_i}\ \forall\Omega_l \in \mathcal{T}_h \right\}\ S_h^{q_i} \subset \mathcal{H}^k(\Omega,\mathcal{T}_h)\ k \geq 1\\
\mathcal{K}_h^{q_i} &= \left\{ v \in S_h^{q_i} \;\middle|\; 0 \leq v \leq 1\ a.e.\ \text{in}\ \Omega \right\}\ \mathcal{K}_h^{q_i} \subset \mathcal{H}_b^k(\Omega,\mathcal{T}_h)\ k \geq 1.
\end{aligned}
\tag{A15}
$$

Let $\{\phi_{lj}, l = 1,\ldots,|\mathcal{T}_h|\ \ j = 1\ldots d(q_i)\}$ be the basis of $S_h^{q_i}$, such that

$$
\begin{aligned}
S_h^{q_i} &= \text{span}\{\phi_{lj}\} \qquad & \phi_{lj} &:\ \Omega_l \to \mathbb{R}\\
\forall v \in S_h^{q_i} \qquad & & v|_{\Omega_l} &= \sum_{j=1}^{d(q_i)} v_{lj}(t)\phi_{lj}(x)
\end{aligned}
\tag{A16}
$$

where $d(q_i)$ is the number of basis functions defined on one element of triangulation ($\Omega_l \in \mathcal{T}_h$), for example, if $q_i = 1$ and Ω_l is a quadrilateral, then $d(1) = 2, 4$ in 1D and 2D domain. After extending the basis functions to the domain, Ω, $\forall k = (l-1)d(q_i) + j$, we write:

$$\begin{aligned}
&\varphi_k : \Omega \to \mathbb{R}, \quad \varphi_k(x) = \begin{cases} \phi_{lj}(x) & x \in \Omega_l \\ 0 & x \notin \Omega_l \end{cases} \\
&\forall v \in S_h^{q_i}, \quad v = \sum_{k=1}^{\mathbb{N}_h^{q_i}} v_k(t)\varphi_k(x), \\
&S_h^{q_i} = \operatorname{span} S_b^i, \quad S_b^i = \left\{\varphi_k^i, j = 1, \ldots, \mathbb{N}_h^{q_i}\right\}
\end{aligned} \tag{A17}$$

where $\mathbb{N}_h^{q_i} = |\mathcal{T}_h| d\,(q_i)$. The primary variables can be written in terms of the basis functions as follows:

$$\mathbf{U}_i(xt) = \sum_k \mathbf{U}_{ik}(t)\varphi_k^i(x) \qquad i \in C \tag{A18}$$

Let $\mathcal{V}_h^i = C\left(\mathbb{T}; S_h^{q_i}\right)$ be the finite dimensional Bochner subspace for $i \in \{p_w, T\}$ and $\mathcal{V}_{hb}^i = C\left(\mathbb{T}; \mathcal{K}_h^{q_i}\right)$ be the finite dimensional Bochner subspace for $i \in \left\{s_g, s_h, \chi_w^M, \chi_g^H, \chi_w^c\right\}$. Now interior and boundary penalty discontinuous Galerkin (IPDG) method for system (23) can be written as follows

Problem 3. *(DG formula) Find* $\mathbf{U} \in \mathcal{V}_h^M \times \mathcal{V}_h^e \times \mathcal{V}_{bh}^H \times \mathcal{V}_{bh}^h \times \mathcal{V}_{bh}^{ncp1} \times \mathcal{V}_{bh}^{ncp2} \times \mathcal{V}_{bh}^c$ *such that* $\forall \psi_j^i \in S_b^i$ *and* $\forall i \in C$

$$\partial_t b^i\left(\mathbf{U}; \psi_j^i\right) + a^i\left(\mathbf{U}; \psi_j^i\right) + a^{\sigma i}\left(\mathbf{U}; \psi_j^i\right) = l^i\left(\mathbf{U}; \psi_j^i\right) + a_D^{\sigma i}\left(\mathbf{U}; \psi_j^i\right) \tag{A19}$$

hold.

A1. Implicit Euler Method

In this section, we apply Implicit Euler method for the system (A19). To do so, we consider a partition $t_0 := 0 < t_1 < \ldots < t_m := t_{\text{end}}$ of the time interval $\mathbb{T}$. By defining $\Delta t_n := t_{n+1} - t_n$, We use finite difference approximation of the time derivative,

$$\partial_t b(\mathbf{U}; \psi) \approx \Delta t_n^{-1}\left(b_h\left(\mathbf{U}^{n+1}; \psi\right) - b_h\left(\mathbf{U}^n; \psi\right)\right) \tag{A20}$$

where $\mathbf{U}^n := \mathbf{U}\,(t_n)$. Let $\mathbb{U}$ be the coefficient vector of the primary variables $\mathbf{U}$ w.r.t basis functions in S_b^i, that is, $\mathbb{U}$ is a row vector with $\mathbf{N}_h = \sum_{i \in C} \mathbb{N}_h^{q_i}$ elements.

Using finite difference approximation of the time derivative (A20), we introduce the residual functional $\mathcal{R}_j^i\left(\mathbb{U}^{n+1}, \mathbf{U}^n\right)$ for every $\psi_j^i \in S_b^i$, $j = 1, \ldots, \mathbb{N}_h^{q_i}$ and $\forall i \in C$ as follows:

$$\begin{aligned}
\mathcal{R}_j^i\left(\mathbb{U}^{n+1}, \mathbf{U}^n\right) \quad := \quad & \Delta t_n^{-1}\left(b^i\left(\mathbf{U}^n; \psi_j^i\right) - b^i\left(\mathbf{U}^{n+1}; \psi_j^i\right)\right) + l^i\left(\mathbf{U}^{n+1}; \psi_j^i\right) \\
& - a^i\left(\mathbf{U}^{n+1}; \psi_j^i\right) - a^{\sigma,i}\left(\mathbf{U}^{n+1}; \psi_j^i\right) + a_D^{\sigma,i}\left(\mathbf{U}^{n+1}; \psi_j^i\right) = 0,
\end{aligned} \tag{A21}$$

The nonlinear residual equations can then be written in compact form as follows:

$$\mathcal{R}\left(\mathbb{U}^{n+1}, \mathbf{U}^n\right) = \left[\mathcal{R}_j^i\left(\mathbb{U}^{n+1}, \mathbf{U}^n\right)\right]_{i,j} = 0, \quad i \in C, \ j = 1, \ldots, \mathbb{N}_h^q, \quad \mathcal{R}\left(\mathbb{U}^{n+1}, \mathbf{U}^n\right) \in \mathbb{R}^{\mathbf{N}_h}. \tag{A22}$$

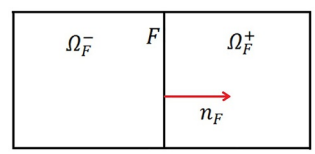

Figure A1. Two neighboring cells with F as common interface.

Data Availability Statement

The published software (Peiraviminaei, 2022), used for the gas hydrate simulation in the study are available at https://doi.org/10.5281/zenodo.6924591 via 10.5281/zenodo.6924591 with open access.

Acknowledgments
A. Peiraviminaei and B. Wohlmuth acknowledge the financial support provided by the Deutsche Forschungsgemeinschaft under the grant number WO 671/11-1. S. Gupta acknowledges funding from the European Research Council (with the grant number 677898 (MARCAN)) under European Union's Horizon 2020 research program. Open Access funding enabled and organized by Projekt DEAL.

References

Archer, D., Buffett, B., & Brovkin, V. (2009). Ocean methane hydrates as a slow tipping point in the global carbon cycle. *Proceedings of the National Academy of Sciences*, *106*(49), 20596–20601. https://doi.org/10.1073/pnas.0800885105

Bastian, P., Heimann, F., & Marnach, S. (2010). Generic implementation of finite element methods in the distributed and unified numerics environment (dune). *Kybernetika*, *46*(2), 294–315. Retrieved from http://eudml.org/doc/197255

Ben Gharbia, I., & Jaffré, J. (2014). Gas phase appearance and disappearance as a problem with complementarity constraints. *Mathematics and Computers in Simulation*, *99*, 28–36. (MAMERN IV–2011: The 4th International Conference on Approximation Methods and Numerical Modeling in Environment and Natural Resources- PART I). https://doi.org/10.1016/j.matcom.2013.04.021

Bey, K. S., Tinsley Oden, J., & Patra, A. (1996). A parallel hp-adaptive discontinuous galerkin method for hyperbolic conservation laws. *Applied Numerical Mathematics*, *20*(4), 321–336. (Adaptive mesh refinement methods for CFD applications). https://doi.org/10.1016/0168-9274(95)00101-8

Biastoch, A., Treude, T., Rüpke, L. H., Riebesell, U., Roth, C., Burwicz, E. B., et al. (2011). Rising arctic ocean temperatures cause gas hydrate destabilization and ocean acidification. *Geophysical Research Letters*, *38*(8). https://doi.org/10.1029/2011gl047222

Blatt, M., Burchardt, A., Dedner, A., Engwer, C., Fahlke, J., Flemisch, B., et al. (2016). The distributed and unified numerics environment, version 2.4. *Archive of Numerical Software*, *4*(100), 13–29. https://doi.org/10.11588/ans.2016.100.26526

Boswell, R., & Collett, T. S. (2011). Current perspectives on gas hydrate resources. *Energy & Environmental Science*, *4*, 1206–1215. https://doi.org/10.1039/C0EE00203H

Brooks, R., & Corey, A. (1964). Hydraulic properties of porous media. In *Colorado State University Hydrology Papers*, Colorado State University.

Burwicz, E., Reichel, T., Wallmann, K., Rottke, W., Haeckel, M., & Hensen, C. (2017). 3-d basin-scale reconstruction of natural gas hydrate system of the green canyon, gulf of mexico. *Geochemistry, Geophysics, Geosystems*, *18*(5), 1959–1985. https://doi.org/10.1002/2017gc006876

Burwicz, E., Rüpke, L., & Wallmann, K. (2011). Estimation of the global amount of submarine gas hydrates formed via microbial methane formation based on numerical reaction-transport modeling and a novel parameterization of holocene sedimentation. *Geochimica et Cosmochimica Acta*, *75*(16), 4562–4576. https://doi.org/10.1016/j.gca.2011.05.029

Cheng, Y., Li, L., Yuan, Z., Wu, L., & Mahmood, S. (2013). Finite element simulation for fluid-solid coupling effect on depressurization-induced gas production from gas hydrate reservoirs. *Journal of Natural Gas Science and Engineering*, *10*, 1–7. https://doi.org/10.1016/j.jngse.2012.10.001

Class, H., Helmig, R., & Bastian, P. (2002). Numerical simulation of non-isothermal multiphase multicomponent processes in porous media: 1. An efficient solution technique. *Advances in Water Resources*, *25*(5), 533–550. https://doi.org/10.1016/s0309-1708(02)00014-3

Class, H., Helmig, R., Niessner, J., & Ölmann, U. (2006). Multiphase processes in porous media. In R. Helmig, A. Mielke, & B. I. Wohlmuth (Eds.), *Multifield problems in solid and fluid mechanics* (pp. 45–82). Berlin, Heidelberg: Springer Berlin Heidelberg. https://doi.org/10.1007/978-3-540-34961-7_2

Cockburn, B., Karniadakis, G. E., & Shu, C. (2000). *Discontinuous galerkin methods* (Vol. 11). Springer Berlin. https://doi.org/10.1007/978-3-642-59721-3

Collett, T., Johnson, A., Knapp, C., & Boswell, R. (2009). *Natural gas hydrates-energy resource potential and associated geologic hazards*. American Association of Petroleum Geologists. https://doi.org/10.1306/M891320

Crutchley, G. J., Mountjoy, J. J., Hillman, J. I. T., Turco, F., Watson, S., Flemings, P. B., et al. (2021). Upward-doming zones of gas hydrate and free gas at the bases of gas chimneys, New Zealand's hikurangi margin. *Journal of Geophysical Research: Solid Earth*, *126*(9), e2020JB021489. https://doi.org/10.1029/2020jb021489

De La Fuente, M., Arndt, S., Marín-Moreno, H., & Minshull, T. A. (2022). Assessing the benthic response to climate-driven methane hydrate destabilisation: State of the art and future modelling perspectives. *Energies*, *15*(9), 3307. https://doi.org/10.3390/en15093307

Dickens, G. R. (2003). Rethinking the global carbon cycle with a large, dynamic and microbially mediated gas hydrate capacitor. *Earth and Planetary Science Letters*, *213*(3), 169–183. https://doi.org/10.1016/s0012-821x(03)00325-x

Fang, H.-L. (2010). A fully coupled thermo-hydro-mechanical model for methane hydrate reservoir simulations. In Y. Chen, L. Zhan, & X. Tang (Eds.), *Advances in environmental geotechnics* (pp. 455–461). Springer Berlin Heidelberg. https://doi.org/10.1007/978-3-642-04460-1_37

Flemings, P., Phillips, S., Boswell, R., Collett, T., Cook, A., Dong, T., et al. (2020). Pressure coring a gulf of mexico deep-water turbidite gas hydrate reservoir: Initial results from the University of Texas–gulf of mexico 2-1 (ut-gom2-1) hydrate pressure coring expedition. *AAPG Bulletin*, *104*(9), 1847–1876. https://doi.org/10.1306/05212019052

Frerichs, D., & John, V. (2021). On reducing spurious oscillations in discontinuous galerkin (dg) methods for steady-state convection-diffusion equations. *Journal of Computational and Applied Mathematics*, *393*, 113487. https://doi.org/10.1016/j.cam.2021.113487

Geissler, W., Gebhardt, C., Gross, F., Wollenburg, J., Jensen, L., Schmidt-Aursch, M., & Krastel, S. (2015). Slope stability, gas hydrates, and methane seepage at the shelf north of svalbard. In *3p arctic: Polar petroleum potential conference & exhibition*. American Association of Petroleum Geologists.

Grozic, J. L. H. (2010). Interplay between gas hydrates and submarine slope failure. In D. C. Mosher, R. C. Shipp, L. Moscardelli, J. D. Chaytor, C. D. P. Baxter, H. J. Lee, & R. Urgeles (Eds.), *Submarine mass movements and their consequences* (pp. 11–30). Springer Netherlands. https://doi.org/10.1007/978-90-481-3071-9_2

Gupta, S., Helmig, R., & Wohlmuth, B. (2015). Non-isothermal, multi-phase, multi-component flows through deformable methane hydrate reservoirs. *Computational Geosciences*, *19*(5), 1063–1088. https://doi.org/10.1007/s10596-015-9520-9

Gupta, S., Wohlmuth, B., & Haeckel, M. (2020). An all-at-once newton strategy for marine methane hydrate reservoir models. *Energies*, *13*(2). https://doi.org/10.3390/en13020503

Holder, G. D., & Angert, P. F. (1982). Simulation of gas production from a reservoir containing both gas hydrates and free natural gas. In (Vol. All days). https://doi.org/10.2118/11105-MS

Huang, Y., Kolditz, O., & Shao, H. (2015). Extending the persistent primary variable algorithm to simulate non-isothermal two-phase two-component flow with phase change phenomena. *Geothermal Energy*, *3*(1), 13. https://doi.org/10.1186/s40517-015-0030-8

Kang, N., Yoo, D.-G., Yi, B., & Park, S.-c. (2015). Distribution and origin of seismic chimneys associated with gas hydrate using 2d multi-channel seismic reflection and well log data in the ulleung basin, east sea. *Quaternary International*, *392*. https://doi.org/10.1016/j.quaint.2015.08.002

Kim, H., Bishnoi, P., Heidemann, R., & Rizvi, S. (1987). Kinetics of methane hydrate decomposition. *Chemical Engineering Science*, *42*(7), 1645–1653. https://doi.org/10.1016/0009-2509(87)80169-0

Kräutle, S. (2011). The semismooth newton method for multicomponent reactive transport with minerals. *Advances in Water Resources*, *34*(1), 137–151. https://doi.org/10.1016/j.advwatres.2010.10.004

Lauser, A., Hager, C., Helmig, R., & Wohlmuth, B. (2011). A new approach for phase transitions in miscible multi-phase flow in porous media. *Advances in Water Resources*, *34*(8), 957–966. https://doi.org/10.1016/j.advwatres.2011.04.021

Lewis, D., & Sager, W. (2012). Salt tectonics and its effect on sediment structure and gas hydrate occurrence in the northwestern gulf of mexico from 2d multichannel seismic data. *GCAGS Journal*, *1*, 27–43.

Liu, X., & Flemings, P. B. (2006). Passing gas through the hydrate stability zone at southern hydrate ridge, offshore Oregon. *Earth and Planetary Science Letters*, *241*(1), 211–226. https://doi.org/10.1016/j.epsl.2005.10.026

Marchand, E., Müller, T., & Knabner, P. (2013). Fully coupled generalized hybrid-mixed finite element approximation of two-phase two-component flow in porous media. Part i: Formulation and properties of the mathematical model. *Computational Geosciences*, *17*(2), 431–442. https://doi.org/10.1007/s10596-013-9341-7

Moridis, G., Moridis, G. J., Kowalsky, M. B., & Pruess, K. (2008). Tough+hydrate v1.0 user's manual: A code for the simulation of system behavior in hydrate-bearing geologic media (tech. Rep.). United States. (Research org. Lawrence berkeley national lab. (LBNL), Berkeley, CA (United States), Sponsor Org. Earth Sciences Division, Report Number: LBNL-149E, Contract Number: DE-AC02-05CH11231). https://doi.org/10.2172/927149

Neumann, R., Bastian, P., & Ippisch, O. (2013). Modeling and simulation of two-phase two-component flow with disappearing nonwetting phase. *Computational Geosciences*, *17*(1), 139–149. https://doi.org/10.1007/s10596-012-9321-3

Nimblett, J., & Ruppel, C. (2003). Permeability evolution during the formation of gas hydrates in marine sediments. *Journal of Geophysical Research*, *108*(B9). https://doi.org/10.1029/2001jb001650

Ostanin, I., Anka, Z., Di Primio, R., & Bernal, A. (2013). Hydrocarbon plumbing systems above the snøhvit gas field: Structural control and implications for thermogenic methane leakage in the hammerfest basin, sw barents sea. *Marine and Petroleum Geology*, *43*, 127–146. https://doi.org/10.1016/j.marpetgeo.2013.02.012

Paganoni, M., Cartwright, J. A., Foschi, M., Shipp, C. R., & Van Rensbergen, P. (2018). Relationship between fluid-escape pipes and hydrate distribution in offshore sabah (nw borneo). *Marine Geology*, *395*, 82–103. https://doi.org/10.1016/j.margeo.2017.09.010

Panfilov, M., & Panfilova, I. (2014). Method of negative saturations for flow with variable number of phases in porous media: Extension to three-phase multi-component case. *Computational Geosciences*, *18*(3), 385–399. https://doi.org/10.1007/s10596-014-9416-0

Peiraviminaei, A. (2022). *apminaei/hydrate-dg: Gas hydrate simulation*. Zenodo. https://doi.org/10.5281/zenodo.6924591

Piñero, E., Marquardt, M., Hensen, C., Haeckel, M., & Wallmann, K. (2013). Estimation of the global inventory of methane hydrates in marine sediments using transfer functions. *Biogeosciences*, *10*(2), 959–975. https://doi.org/10.5194/bg-10-959-2013

Portnov, A., Cook, A. E., Sawyer, D. E., Yang, C., Hillman, J. I., & Waite, W. F. (2019). Clustered bsrs: Evidence for gas hydrate-bearing turbidite complexes in folded regions, example from the perdido fold belt, northern gulf of mexico. *Earth and Planetary Science Letters*, *528*, 115843. https://doi.org/10.1016/j.epsl.2019.115843

Riboulot, V. (2018). Geomorphology of gas hydrate-bearing pockmark, *04*, 37–48. https://doi.org/10.1002/9781119451174.ch4

Schmidt, C., Gupta, S., Rüpke, L., Burwicz-Galerne, E., & Hartz, E. H. (2022). Sedimentation-driven cyclic rebuilding of gas hydrates. *Marine and Petroleum Geology*, *140*, 105628. https://doi.org/10.1016/j.marpetgeo.2022.105628

Serié, C., Huuse, M., & Schødt, N. H. (2012). Gas hydrate pingoes: Deep seafloor evidence of focused fluid flow on continental margins. *Geology*, *40*(3), 207–210. https://doi.org/10.1130/G32690.1

Waage, M., Portnov, A., Serov, P., Bünz, S., Waghorn, K. A., Vadakkepuliyambatta, S., et al. (2019). Geological controls on fluid flow and gas hydrate pingo development on the barents sea margin. *Geochemistry, Geophysics, Geosystems*, *20*(2), 630–650. https://doi.org/10.1029/2018gc007930

Wohlmuth, B. (2011). Variationally consistent discretization schemes and numerical algorithms for contact problems. *Acta Numerica*, *20*, 569–734. https://doi.org/10.1017/S0962492911000079

Wu, Y.-S., & Forsyth, P. A. (2001). On the selection of primary variables in numerical formulation for modeling multiphase flow in porous media. *Journal of Contaminant Hydrology*, *48*(3), 277–304. https://doi.org/10.1016/s0169-7722(00)00180-7

Wuebbles, D. J., Fahey, D. W., Hibbard, K. A., DeAngelo, B., Doherty, S., Hayhoe, K., et al. (2017). Executive summary. In D. J. Wuebbles, D. W. Fahey, K. A. Hibbard, D. J. Dokken, B. C. Stewart, & T. K. Maycock (Eds.), *Climate science special report: Fourth national climate assessment, volume i* (pp. 12–34). U.S. Global Change Research Program. https://doi.org/10.7930/J0DJ5CTG

Yoo, D.-G., Kang, N., Yi, B., Kim, G., Ryu, B.-J., Lee, K., et al. (2013). Occurrence and seismic characteristics of gas hydrate in the ulleung basin, east sea. *Marine and Petroleum Geology*, *47*, 236–247. https://doi.org/10.1016/j.marpetgeo.2013.07.001

You, K., Flemings, P., Malinverno, A., Collett, T., & Darnell, K. (2019). Mechanisms of methane hydrate formation in geological systems. *Reviews of Geophysics*, *57*(4), 1146–1196. https://doi.org/10.1029/2018rg000638

You, K., Summa, L., Flemings, P., Santra, M., & Fang, Y. (2021). Three-dimensional free gas flow focuses basin-wide microbial methane to concentrated methane hydrate reservoirs in geological system. *Journal of Geophysical Research: Solid Earth*, *126*(12), e2021JB022793. https://doi.org/10.1029/2021jb022793

Yu, M., Li, W., Yang, M., Jiang, L., & Song, Y. (2017). Numerical studies of methane gas production from hydrate decomposition by depressurization in porous media. *Energy Procedia*, *105*, 250–255. (8th International Conference on Applied Energy, ICAE2016, 8-11 October 2016, Beijing, China). https://doi.org/10.1016/j.egypro.2017.03.310

Zander, T., Haeckel, M., Berndt, C., Chi, W.-C., Klaucke, I., Bialas, J., et al. (2017). On the origin of multiple bsrs in the danube deep-sea fan, black sea. *Earth and Planetary Science Letters*, *462*, 15–25. https://doi.org/10.1016/j.epsl.2017.01.006